Centro de Investigación en Materiales Avanzados, S.C.

2D materials and semiconducting polymers: from synthesis to devices for energy applications

Thesis that as a Requirement to obtain the Doctorate Degree in Nanotechnology presents:

M. Sc. Ulises Antonio Méndez Romero

Thesis Director:
Dra. Liliana Licea Jiménez

Thesis Co-Director:
Dr. Sergio Alfonso Pérez García

External Director:
Prof. Ergang Wang

Apodaca, N.L., México 2020

2D materials and semiconducting polymers: from synthesis to devices for energy applications

List of research articles

‡Equal contribution, *Corresponding Authors

Paper I (I.F. 8.821)

"Functionalized reduced graphene oxide with tunable band gap and good solubility in organic solvents"

U.A. Méndez-Romero, S.A. Pérez-García*, X. Xu, E. Wang*, L. Licea-Jiménez*, *Carbon* **2019,** 146, 491-502. doi:10.1016/j.carbon.2019.02.023

Paper II (I.F. 4.056)

"Fluorinated Photovoltaic Materials for High-Performance Organic Solar Cells"

Q. Fan, **U.A. Méndez-Romero**, X. Guo, E. Wang*, M. Zhang*, Y. Li, *Chemistry – An Asian Journal* **2019**, 14(18) 3085-3095. doi:10.1002/asia.201900795

Paper III (I.F. 27.054)

"Mechanically Robust All-Polymer Solar Cells from Narrow Band Gap Acceptors with Hetero-Bridging Atoms"

Q. Fan‡, W. Su‡, S. Chen, W. Kim, X. Chen, B. Lee, T. Liu, **U.A. Méndez-Romero**, R. Ma, T. Yang, W. Zhuang, Y. Li, Y. Li, T.-S. Kim*, L. Hou*, C. Yang*, H. Yan, D. Yu, E. Wang*

Joule **2020**,4 (3), 658-672. doi:10.1016/j.joule.2020.01.014

Paper IV (I.F. 12.130)

"Weak Makes It Powerful: The Role of Cognate Small Molecules as an Alloy Donor in 2D/1A Ternary Fullerene Solar Cells for Finely Tuned Hierarchical Morphology in Thick Active Layers"

Q. Fan, T. Liu*, M. Zhang, W. Su, **U.A. Méndez-Romero**, T. Yang, X. Geng, L. Hou, D. Yu, F. Liu*, H. Yan*, E. Wang*

Small Methods **2020**, 4(3)1900766. doi:10.1002/smtd.201900766

Paper V (I.F. 3.119)

"Lateral size reduction of graphene oxide preserving its electronic properties and chemical functionality"

U.A. Méndez-Romero, S.A. Pérez-García*, Q. Fan, E. Wang*, L. Licea-Jiménez*, *RSC Advances* **2020** Accepted

Paper VI (I.F. 25.245)

"Highly Stable Indacenodithieno[3,2-b]thiophene-Based Donor-Acceptor Copolymers for Hybrid Electrochromic and Energy Storing Applications"

P. Murto‡, S. Elmas‡, **U.A. Méndez-Romero**, Y. Yin, M. Mone, G. Andersson, M.R. Andersson*, E. Wang*

Advanced Energy Materials **2020** Submitted

Paper VII (I.F. 5.278)

"Impact of graphene oxide properties based on storage conditions"

U.A. Méndez-Romero, M.A. Velasco-Soto*, L. Licea-Jiménez*, S.A. Pérez-García*

Journal of Industrial and Engineering Chemistry **2020** Submitted

Paper VIII
"Selectively oxidized graphene for applications in energy storage and organic electronics"
A. Méndez-Reséndiz‡, **U.A. Méndez-Romero**‡*, R.A. Mendóza-Jiménez, S.A. Pérez-García*, E. Wang*, L. Licea-Jiménez*
(2020) To be Submitted

Book Chapter

L. Licéa-Jiménez, **U.A. Méndez-Romero**, A. Méndez-Reséndiz, A.R. Vázquez-Velázquez, R.A. Mendóza-Jiménez, D.F. Rodríguez-Díaz, S.A. Pérez-García *"Chapter 5: Polymer coatings based on nanocomposites"* in Polymer Coatings: Technologies and Applications (2020) **CRC Press**

Index

Abstract

For a sustainable society, the supply of cheap and green energy is indispensable, which requires not only renewable energy source but also a green solution for energy storage. In this regard, considering that renewable energy sources are intermittent, is crucial to storage the produced energy. Supercapacitors are excellent candidates because they have numerous advantages as high-power density, ultra-fast charge-discharge, and long cycle life. However, the energy density is its main drawback. In this context, the proper use of 2D materials' properties to take advantage, *i.e.* of the conductivity and redox activity, is possible to increase the said energy density of the supercapacitor. In the case of energy production, solar cells have the possibility to satisfy the energy demand, in particular the organic photovoltaics (OPVs), because of their low cost, light weight and easy fabrication, when compared to the silicon solar cells. However, the OPVs need even more improvements in the active layer, in order to completely success in the market.

The main goal of the present work is to contribute to the area of renewable energy production and storage, trough the precise engineering of 2D materials and semiconducting polymers. Thus, four different type of graphene-based materials, two kind of Transition Metal Dichalcogenides (TMDs) and a semiconducting polymer were synthesized in order to successfully develop supercapacitors and OPVs. The best supercapacitor showed a 16000 mFg^{-1}, when charged at 5mV s^{-1} and more interesting, the synergy between the 2D materials allowed to have a capacitance retention above 75% at 1000 mV s^{-1} and almost 20% at 50 000 mV s^{-1}. Also, the capacitance retention after 30 000 cycles of charge-discharge was higher than 98%. In the case of the OPVs, the synthesized 2D materials and the semiconducting polymer presented more than 400% efficiency compared to the commercial materials normally used.

Finally, the chemical, optoelectronic and morphological characterization was performed by means of SEM, DLS, XRD, UV-Vis, Cyclic Voltammetry, Raman and XPS.

Introduction

The most critical issue that needs to be solve in the near future is energy production.(Smalley, 2005) Fossil fuels have been widely used to meet the demands of mobility, product development and mainly electric power production. Nevertheless, as this type of fuel is a finite resource and generates pollution, it is imperative to develop alternative technologies to satisfy energy demand.(Krebs, 2008)

One of the most explored technologies that eventually could overcome the energy problem are solar cells or photovoltaic cells (PVs). These devices convert the electromagnetic energy radiation from the sun into electrical energy, which in principle, could supply the energy needs with relative ease.(Krebs, 2008)

The sun puts out 3.8×10^{23} kilowatt-hours of energy every hour, see Figure 1. From that, 170 000 Tera Watts (TW) strike Earth every moment, nearly one-third of which are reflected back into space, leaving “just” 120 000 TW. It means that every hour, Earth's surface receives more energy from the sun than humans use in a year. In fact, covering 1.7 % of the Earth with 1 % power conversion efficiencies (PCE, which is the ratio between the maximum power in watts that the cell produces, divided by the power in watts of the incident light) PVs would provide 20 TW of power, nearly twice the world's consumption rate of fossil energy and the equivalent to 20 000 nuclear fission plants of 1GW.(Armaroli & Balzani, 2007; Service, 2005) Unfortunately, PVs currently turn sunlight into 0.3 TW of electricity.(Ludin et al., 2018)

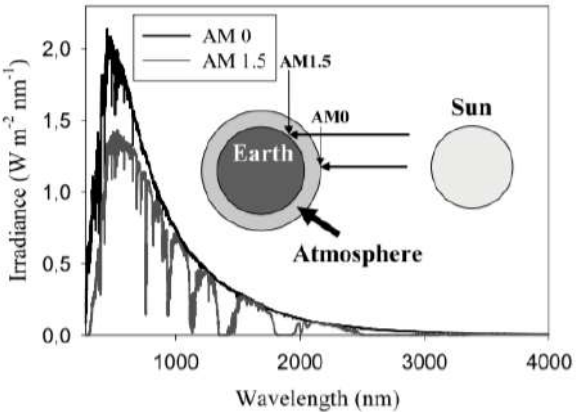

Figure 1. Solar irradiance spectrum.(Krebs, 2008)

In general, conventional PVs are silicon-based p-type and n-type semiconductor junctions, with maximum PCE around 25.11%, and the commercial ones around 16%. (Ru et al., 2020) However this PV type shows as main drawback a high cost.(Markavart, 2005)

Based on the above, alternatives have been explored with organic compounds, *i.e.*, organic photovoltaics (OPVs)(Thompson & Fréchet, 2008). In this type of cells, the active layer, which is a blend film of conjugated polymers (as the donors) and fullerene derivatives ($PC_{61}BM$, $PC_{71}BM$, indene-C_{60} bisadduct (ICBA), etc.)(Wadsworth et al., 2019) (as the acceptors), have attracted considerable attention in both academia and industry because of their low cost, light weight, transparency easy fabrication, and potential use in flexible devices and as promising technology for the production of renewable energy.(Fan et al., 2018)

In this context, because the renewable energy sources are intermittent, other important aspect to consider, are energy storage devices, such as supercapacitors, which have advantages compared to batteries: providing high power density (10 $kWkg^{-1}$), charge/discharge time in seconds and long cycle life. In general, there are two types. One is the electrical double layer capacitor (EDLC), which stores energy via an electrostatic process, *i.e.*, charges are accumulated at the electrode/electrolyte interface through polarization. The second type of

supercapacitor is the pseudocapacitor, based on fast redox reactions of compounds in the electrode. The common electrode materials are metal oxides and conducting polymers. This type of electrode offers higher specific capacitance per unit surface area.(Huang et al., 2012)

For supercapacitors, it is essential to use electrode materials with good conductivity and large specific surface areas such as graphene-based materials. The graphene-based materials, in particular rGO, are advantageous in terms of the chemically active surface with large specific area, good conductivity, low cost, and mass production with solution-based processability. (Huang et al., 2012; Méndez-Romero et al., 2017)

For OPVs active layers, the requirements are more complex. There are 3 main parameters to adjust in order to develop a high-performance device: material design, device engineering and morphology optimization. In the case of material design, it is crucial to design low bandgap acceptor and donor, to have a good absorption match with the solar spectrum (seen in Figure 1). The device engineering is related to fabrication, for instance annealing, the thickness of each layer and the type of materials that can be use, for example, instead of PEDOT-PSS, ZnO can be use and MoO_3 could replace the LiF layer. Finally, the morphology optimization of the active layer depends on the solubility, size of the donor:acceptor domains and the ratio between them.(Cui et al., 2019)

I. Materials and Devices

1. Graphene and Graphene-based Materials

Graphene, is a single layer of carbon atoms bonded in a hexagonal array (honeycomb like, see Figure 2,) with sp^2 hybridization that exhibits a vast number of outstanding characteristics, making it one of the most promising two-dimensional (2D) material. In general, the properties of 2D materials arise from the quantum confinement effects along z-axis, leading to unusual electronic and surface characteristics. For instance, graphene possesses high optical transmittance (>97% from 400 to 1000 nm), thermal conductivity (~5000 $Wm^{-1}K^{-1}$), high Young's modulus (~1.0 TPa), large specific surface area (2630 $m^2\ g^{-1}$) and extraordinary carrier mobility (2.5 x 10^5 $cm^2\ V^{-1}\ s^{-1}$), attributed besides of quantum confinement to the interaction of electrons with the periodic potential of graphene's honeycomb lattice. In this way, the particular crystalline structure and the said sp^2 domain gives rise to relativistic massless Dirac fermion behavior of electrons that obey Dirac's equation instead of the Schrödinger's equation.(Geim & Novoselov, 2010; Novoselov et al., 2005; Novoselov et al., 2004)

Moreover, graphene is a zero-band gap material due to its π-band (bonding π molecular orbital) and π^*-band (antibonding π^* molecular orbital) having a characteristic shape of Dirac cones, touching at the Dirac points.(Novoselov et al., 2005) Hence, most attention is focused on graphene applications for transparent and flexible electrodes.(Garg et al., 2017) Nevertheless, certain applications, such as organic electronics and OPVs require particular properties, as specific band gap (E_g), highest occupied molecular orbital (HOMO) and lowest unoccupied molecular orbital (LUMO) energy levels, good solubility in organic solvents as well as a low cost that graphene can achieve when is subjected to certain chemical modifications, in other words a graphene-based material.(Méndez-Romero et al., 2019)

Based on the aforementioned properties, there is a variety of research on graphene-based materials applied in green energy such as fuel cell, solar cell,

lithium-ion batteries (LIBs), supercapacitor, dye-sensitized solar cells (DSSC), and photo- electrochemical cell for hydrogen evolution via water splitting.(Tsang et al., 2020) In particular, previous work related to the use of graphene derivatives in OPVs mainly focuses on graphene as the hole transporting layer (HTL), the electron transporting layer (ETL) and the active layers, showing satisfactory results. (Bernardi et al., 2012; Chen et al., 2015; Jeon et al., 2012; Qu et al., 2013)

Graphene oxide (GO) is the most studied graphene-based material, which essentially is graphene with oxygen functional groups: hydroxyl, carboxyl, epoxy and carbonyl. GO exhibits a wide optical band gap (E_g^{opt}) of 3 eV and therefore, a HOMO and LUMO levels.(Méndez-Romero et al., 2019) The poor solubility in organic solvents, mismatching energy levels, large E_g as well as high electrical resistance ($\sim 10^{11}$ Ω)(Jung et al., 2008) due to the loss of crystallinity in GO, limit its applications in organic electronics.

Since sp^2 domains and E_g in GO are related to C/O ratio, a promising strategy will be to reduce the amount of oxygen by chemical reduction reactions, which leads to another graphene-based material: reduced graphene oxide (rGO) with a narrower E_g and therefore, higher conductivity ($\sim 7.5 \times 10^4$ S m^{-1}).(Garg et al., 2014) These chemical reactions can be carried out with harmful compounds like $NaBH_4$, N_2H_4 but also with innocuous fructose in aqueous dispersions, however, both methods have the inconvenience of restacking of the layers, which results in poor solubility. (Velasco-Soto et al., 2015)

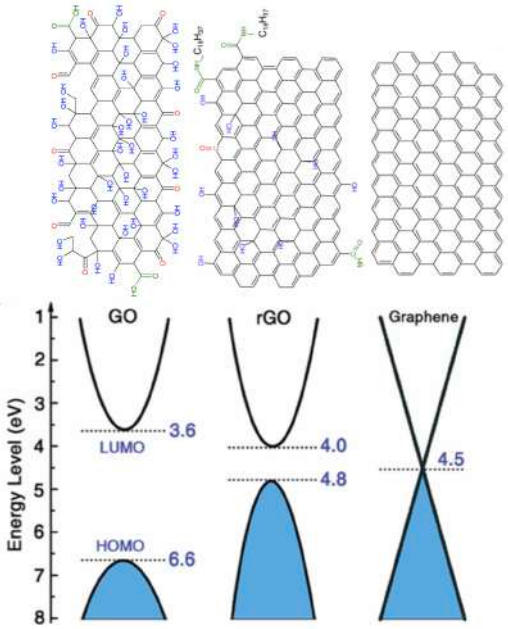

Figure 2. Structure of GO, rGO and graphene as well as their energy levels.(Zheng et al., 2015)

2. Transition Metal Dichalcogenides

Other ground-breaking 2D materials are transition metal dichalcogenides (TMDs) which are semiconductors of the type MX_2, where M is a transition metal atom (*e.g.* Mo or W) and X is a chalcogen atom (as S, Se or Te) such as MoS_2, $MoSe_2$, and WS_2. As already said, graphene is attractive because of its numerous interesting properties, but its lack of an electronic E_g has motivated the search for 2D materials with semiconducting character. Due to its robustness, MoS_2 is the most studied material in this family. TMDs exhibit a unique combination of atomic-scale thickness, direct bandgap and favorable electronic and mechanical properties, which make them interesting for fundamental studies and for applications in high-end electronics, spintronics, optoelectronics, energy harvesting, flexible electronics, DNA sequencing and energy storage. (Manzeli et al., 2017)

TMDs can be found in different structural phases resulting from different coordination spheres of the transition metal atoms. The two common structural configurations are either trigonal prismatic (2H) or octahedral (1T) (See Figure 3a)). The existence of the two phases, in either stable or metastable form, and other

properties of TMDs are summarized in the ‘periodic table’ shown in Figure 3 b).(Manzeli et al., 2017)

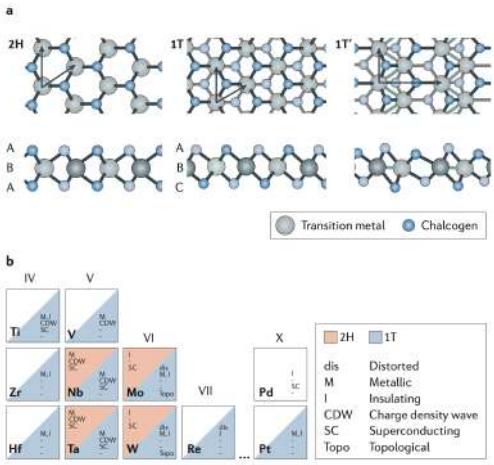

Figure 3. a) Atomic structure of single layers of transition metal dichalcogenides (TMDs) in their trigonal prismatic (2H), distorted octahedral (1T) and dimerized (1T') phases. b) ‘Periodic table’ of known layered TMDs, organized based on the transition metal element involved.(Manzeli et al., 2017)

The enormous variety of chemical compositions and structural phases of TMDs results in a broad range of electronic properties, both from the point of view of the band structure character. By focusing on the basic features of the band structure of TMDs made by group VI transition metals Mo and W combined with S and Se, it is possible to stablish a trend. The evolution of the band structure of 2H-MoS_2 as calculated by density functional theory (DFT), reducing its thickness from bulk to monolayer is shown in Figure 4. The positions of the valence and conduction bands change with decreasing thickness and the indirect E_g semiconductor bulk material turns into a direct E_g semiconductor monolayer. The calculated values for the E_g of bulk and monolayer 2H-MoS_2 are 0.88 and 1.71 eV, respectively.(Manzeli et al., 2017)

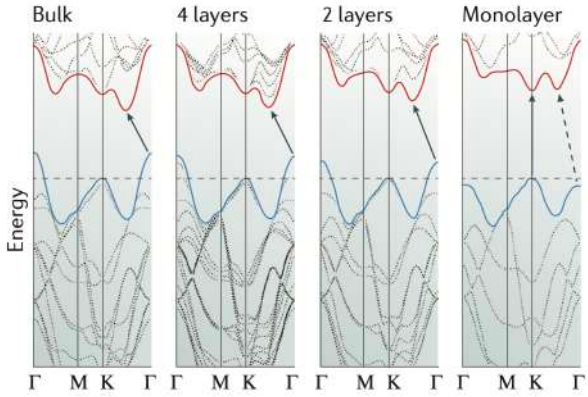

Figure 4. Evolution of the band structure of 2H-MoS_2 calculated for samples of decreasing thickness.(Manzeli et al., 2017)

3. Semiconducting Polymers

In a molecule with at least two adjacent sp^2 hybridized carbon atoms, the sp^2 hybrid orbitals form single (σ) bonds, whereas the non-hybrid *p*-orbitals form a double (π) bond between the carbon atoms, as shown for ethene in Figure 5a). In a larger structure, such as buta-1,3-diene (Figure 5b)), the π-bond electrons can diffuse (*i.e.* delocalize) along the neighboring *p*-orbitals, known as conjugated system. The conjugated *p*-orbitals together form new molecular orbitals, which share the electron density depending on the phase of each *p*-orbital. In the case of buta-1,3-diene, a total of four molecular π-orbitals are formed, as illustrated in Figure 5c). The π-electrons occupy the two lower-energy (in-phase, bonding) molecular orbitals, leaving the two higher-energy (out-of-phase, antibonding) molecular orbitals unoccupied. Thus, the naming HOMO -1, HOMO, LUMO, and LUMO+1, according to their occupation and increasing energy, respectively. The energy difference between the HOMO and LUMO is called band gap. Interestingly, the shared π-electrons between the *p*-orbitals reduce rotational torsion between the carbon atoms, which planarizes the conjugated structure.(Anslyn & Dougherty, 2006; Hollas, 2004)

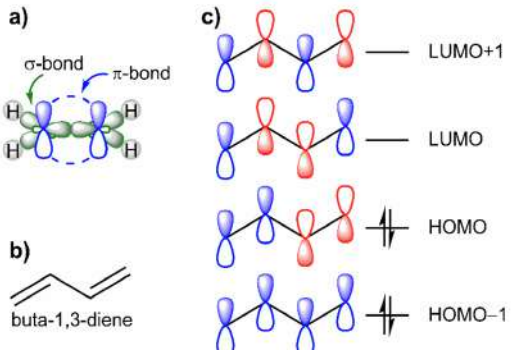

Figure 5. a) σ- and π-bonds in ethene molecule; b) Chemical structure of buta-1,3-diene and c) illustration of the conjugated *p*-orbitals.(Anslyn & Dougherty, 2006)

The ultimate advantage of conjugated polymers are their tunable properties such as band gap, molecular energy levels, carrier mobility, morphology, among others. A general strategy to synthesize a conjugated polymer is by combining an electron-rich monomer (donor) and electron-deficient monomer (acceptor), in order to polymerize a D–A alternating conjugated polymer. When the donor monomer is bonded to the acceptor monomer, results into a D-A conjugated polymer that has a linear combination of molecular orbitals, *i.e.*, the HOMO of the polymer is similar to the HOMO of the donor monomer, while the LUMO of the polymer is similar to the LUMO of the acceptor monomer, resulting into a lower band gap and therefore capable of use wider solar spectrum, as seen in Figure 6.(Anslyn & Dougherty, 2006)

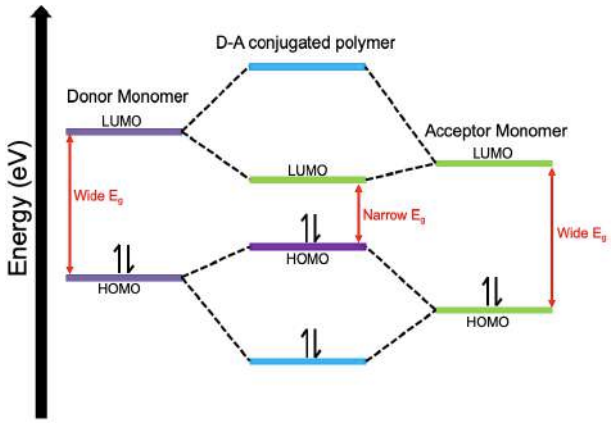

Figure 6. Linear combination of frontier molecular orbitals.(Anslyn & Dougherty, 2006)

Some of the most promising semiconducting (conjugated) polymers with low band gap and high PCE, combines an electron-rich unit indacenodithieno[3,2-

b]thiophene (IDTT) and an electron-deficient unit [1,2,5] thiadiazolo[3,4-f]isoindole-5,7-dione (TID) to get the polymer poly[indacenodithieno[3,2-b]thiophene-alt-6-(2-ethyl-hexyl)-4,8-[1,2,5]thiadiazolo[3,4-*f*]isoindole-5,7-dione] (PIDTT-TID), which is polymerized by Stille coupling reaction, see Figure 7. (Wang et al., 2016). Good photovoltaic performance with PCE over 13.5% has been obtained in OPVs based on D–A copolymers.(Fan et al., 2018)

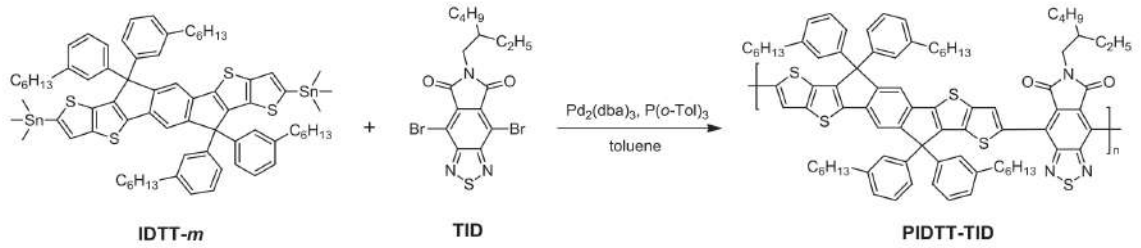

Figure 7. Synthetic route for low band gap D-A semiconducting polymer.(Wang et al., 2016).

Halogenation is another approach to improve and control the properties of the conjugated polymers. The halogen atoms are an electron-withdrawing group, halogen substituents of photovoltaic materials do not increase undesirable large steric hindrance caused by other electron-withdrawing groups such as cyano or ester groups. The main motivation to introduce halogens into donor materials is to lower the HOMO level, with the aim to obtain a higher open-circuit voltage (V_{OC}) in OPVs. In addition, halogenated materials usually have many intramolecular and intermolecular noncovalent interactions, such as F···H/N/O/F/S/π. Therefore, molecular halogenation will significantly affect the photo-electronic properties of the materials. For example, compared with their non-halogenated analogues, halogenated molecules show improved planarity, enhanced extinction coefficients, better molecular orientation, higher charge carrier mobility, and improved morphological miscibility.(Fan et al., 2019)

4. Organic Photovoltaics

The most efficient OPVs are based in the bulk heterojunction concept (BHJ), see Figure 8 (Yu et al., 1995). In this type of solar cell, electron donor material (usually a polymer like poly[3-hexylthiophene], P3HT) is mixed with an electron acceptor material (derived from fullerenes like [6,6]-phenyl-C61-butyric acid methyl ester, $PC_{61}BM$) in an organic solvent (*e.g.*1,2-dichlorobenzene) and subsequently deposited by spin coating on cathode made of indium-tin oxide (ITO) substrate previously placed on a glass or polyethylene terephthalate (PET) substrate. During evaporation of the solvent and subsequent annealing treatments, a bicontinuous microphase is generated, thus giving rise to the creation of a large interfacial area between the donor material and the acceptor material: the said BHJ, also called the photoactive layer or simply the active layer. A layer that prevents the transport of holes, such as lithium fluoride (LiF) is added and as last step a metal anode (*e.g.* aluminum), these two layers are deposited by sputtering, inside a glove box in N_2 atmosphere(Krebs, 2008).

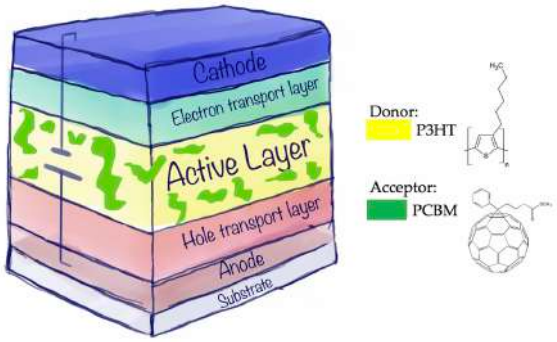

Figure 8. Typical OPV-BHJ architecture.

The common feature of materials used as active layer in OPVs is that they are small polymeric molecules, soluble in organic solvents with conjugated bonds alternating sp^2 hybridization, which allows the continuous transport of electrons along the molecular structure. In addition, these materials must have adequate values of HOMO, LUMO and E_g. It is well known that, the PCE of an OPV is determined by four key factors: its open-circuit voltage (V_{OC}), short-circuit current (J_{SC}), power in (P_{in}) and fill factor (FF) as described in Equation 1.

$$PCE = \frac{P_{out}}{P_{in}} = FF = \frac{J_{sc}V_{oc}}{P_{in}} = \frac{J_m V_m}{J_{sc}V_{oc}}$$

Equation 1. Power conversion efficiency. (Thompson & Fréchet, 2008)

Where J_m and V_m are the maximum current and maximum potential density, respectively. These values are obtained through I-V curves, carrying out 2 measurements, one in darkness and the other under illumination as shown in Figure 9.

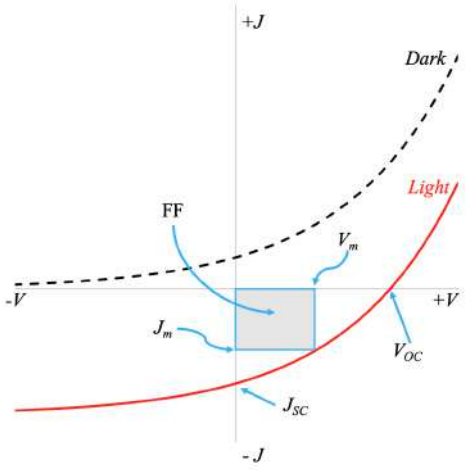

Figure 9. I-V Curve from a solar cell in dark and under illumination and the parameters obtained from it.(Thompson & Fréchet, 2008)

These parameters are closely associated to the optoelectronics of the polymer and the nanocomposite of the active layer. In particular, V_{OC} is directly determined by the energy difference between the HOMO level of the electron donor (polymer) and the LUMO level of the acceptor (fullerene derivatives).(Zhang et al., 2015)

Based on these requirements, one type of material that is currently studied as an alternative in OPVs, is graphene-based materials. Some of the GO challenges are: to tailor the proper set of energy levels, to improve the conductivity, to improve solubility in organic solvents, and to reduce the band gap. Enabling its use instead of common organic semiconductors in OPVs, *e.g.* fullerene derivatives, which

present wide limitations as: low absorption, morphological instability and high costs. At the end, these restrains generate a strong requirement to develop new semiconducting materials.(Méndez-Romero et al., 2019; Méndez-Romero et al., 2017)

A theoretical study on PV devices based on just two stacked monolayers (see Figure 10), demonstrate that 1 nm thick active layers can reach PCE of ~1% but more interesting, with a power density around 2.5 MW/kg.(Bernardi et al., 2013)

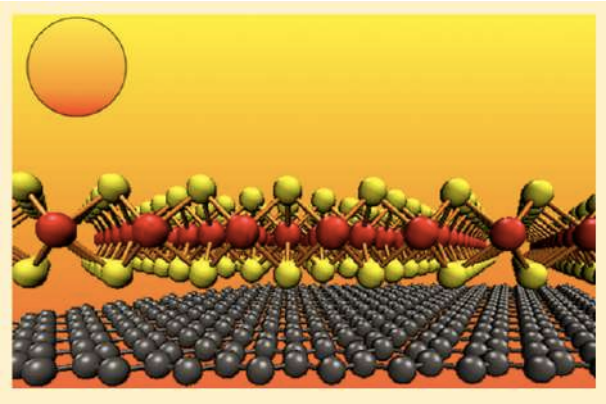

Figure 10. 2D active layer.(Bernardi et al., 2013)

A great opportunity area is related to study the interaction of 2D materials and polymers blends as active layers in OPVs. As previously stated, graphene-based materials exhibit a vast thermal conductivity. Thus, the incorporation of such materials in the OPVs' photoactive layer, could mitigate heat-related degradation effects due to prolonged solar illumination. More importantly, due to their extremely high aspect ratio, 2D materials are perfectly fitted to promote migration of electrons along their *x-y* plane. In this respect, 2D materials are anticipated to be utilized for the efficient exciton separation and charge transport when blended with conjugated polymers, because of their large surface area for donor:acceptor interfaces and continuous pathway for the electron transfer.

As an example of graphene-based material as acceptor in OPVs, a photochemical functionalization of GO, by pulsed laser irradiation allowed to get a tunable bandgap electron acceptor system, named as laser GO-ethylene-dinitro-

benzoyl (LGO-EDNB). The fabricated device got a 2.4% efficiency as seen in Figure 11.(Stylianakis et al., 2015)

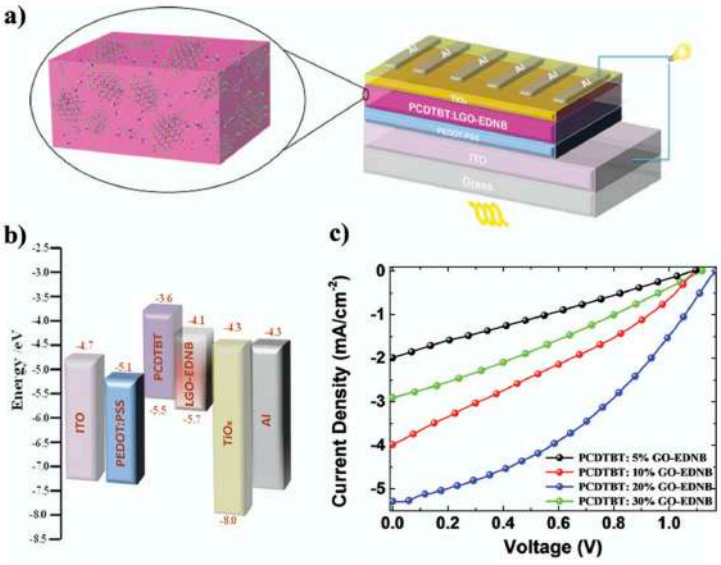

Figure 11. Schematic illustration of a BHJ OPV device with a graphene-based material as acceptor. b) Energy level diagram for all the materials in the OPV. c) J-V features for the OPVs with different amount of graphene-based materials in the BHJ.(Stylianakis et al., 2015)

5. Supercapacitors

Another application is related to the energy storage devices like supercapacitors. Compared to batteries, supercapacitors exhibit higher-power density but lower energy density. Supercapacitors are one application where 2D materials can greatly increase performance and efficiency. Supercapacitors are unique because they provide a much higher power density than conventional batteries, while having a higher energy density than regular capacitors maintaining almost limitless cycling durability. The charge storage mechanism in supercapacitors can be divided into two groups: electric double-layer capacitors (EDLCs) and pseudocapacitors. EDLCs store energy through the accumulation of ions at the interface between the electrode and the electrolyte, and because of this, their performance is dependent on the surface area of the electrode, pore size, and electrical conductivity. Pseudocapacitors, on the other hand, use fast reversible redox reactions at the electrode–electrolyte interface, resulting in Faradaic charge

transfer. EDLCs have the advantage of almost limitless cyclability with minor degradation, but low specific capacitances when compared to pseudocapacitors. Because, the latter have much higher specific capacitance often suffer from performance degradation from repeated charge–discharge cycles. (Li et al., 2009; Volkov et al., 2017)

The stored energy (*E*) in a capacitor is proportional to the capacitance (*C*) and voltage (*V*), where the maximum operating voltage depends on the stability of the electrolytes. In contrast, the capacitance relies on the active material from the electrodes.(Li et al., 2009; Volkov et al., 2017)

$$E = CV^2$$

Equation 2. Stored energy in a capacitor.

The specific capacitance (C_{sp}) of the thin film electrodes capacitors can be calculated from the *CV* plots using Equation 3.(Li et al., 2009; Volkov et al., 2017)

$$C_{sp} = \frac{\int I(V)dV}{vA\Delta V}$$

Equation 3. Stored energy in a capacitor.

Where $\int I(V)dV$ is the integral of the *CV* plot, v is the scan rate (V/s), A is the area of the electrode (cm^2) and ΔV is the potential range of the *CV* scan.(Li et al., 2009; Volkov et al., 2017)

As an example, to improve the energy density while maintaining the high-power density from the graphene/metal oxide hybrid electrode, an asymmetric capacitor system was employed (see Figure 12). As a result, a maximum energy density of 30.4 $Whkg^{-1}$ for this asymmetric capacitor was achieved, a higher value than the results obtained from the symmetric one, *i.e.* with graphene (or graphene/MnO_2) as both the positive and negative electrodes.(Wu et al., 2010)

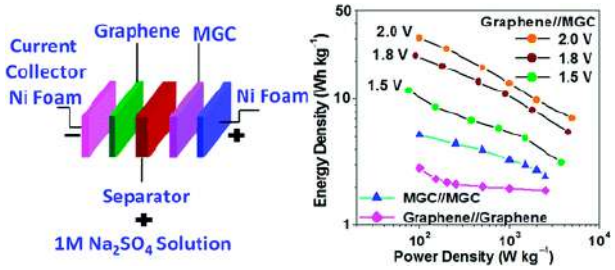

Figure 12. Schematic of the assembled structure of asymmetric supercapacitor and the Energy and power densities plot.(Wu et al., 2010)

II. Hypothesis

1. The chemical and physical modification of 2D materials will enable its incorporation into the active layer of organic photovoltaic devices. The chemical modification of 2D materials through functionalization by alkyl amines will allow good dispersibility, at least [5 mg mL^{-1}] in organic solvents. The physical modification through ultrasonic probe will allow to obtain at least bi-layered TMDs materials and will reduce the lateral dimension at smaller values than 500 nm. Both modifications will promote a shift in the band gap below 1.8 eV in order to use all the visible spectrum. After the molecular engineering in 2D materials, the size, solubility and band gap will be suitable for its incorporation into a tailored *ad-hoc* semiconducting polymer matrix as an active layer of hybrid photovoltaics, overcoming the stability and with a PCE over 1%.
2. Based on the vast and different properties of 2D materials, graphene-based and TMDs, it will be possible to use them into energy storage devices, such as supercapacitors. By the appropriated combination of the synthesized 2D materials into a nanocomposite electrode, it will be possible to take advantage of the high conductivity and stability of the graphene-based materials in conjunction with the different oxidation states of the metal in TMDs, *i.e.*, capacitance and pseudocapacitance respectively, will create a synergistic effect that will lead into a boost in the energy density. The 2D materials-based electrodes will promote a specific capacitance over 10 000 mF g^{-1}.

III. Objectives

1. Main objective

To chemically tailor materials and to develop devices for energy applications based on hybrid 2D materials and semiconducting polymers.

2. Specific objectives

2.1 To synthesize and to functionalize graphene-based materials (GBMs) and transition metal dichalcogenides (TMDs) controlling their resulting properties.

2.2 To synthesize an *ad-hoc* semiconducting polymer to use it as electron-donor and polymer matrix for GBMs and TMDs.

2.3 To implement an experimental method to control the dispersibility of GBMs and TMDs in the photoactive layer or electrode.

2.4 To characterize the electronic, optical, chemical and morphological properties of all the synthesized materials.

2.5 To develop OPV devices for their characterization.

2.6 To develop energy storage devices for their characterization.

Methodology

Based on the planned objectives, different methodologies where developed. In the case of 2D materials, four different graphene-based materials were synthesized: 1. Reduced lateral size graphene oxide, 2. Reduced graphene oxide functionalized by octadecylamine, 3. Selectively oxidized graphene and 4. Exfoliated graphene. Two different TMDs: 1. Molybdenum disulfate and 2. Molybdenum diselenide. Also, an *ad-hoc* semiconducting polymer was synthesized. Organic solar cells and supercapacitors were fabricated with the synthesized materials.

As previously stated in the introduction, graphene is not suitable for its direct use in the active layer of the organic solar cells or as electrode for supercapacitors. In order to use it, different approaches were done. All the methods employed followed the top-down strategy, to obtain materials in enough quantities (grams). The oxidation of graphite to produce graphene oxide (GO), make it water soluble and originates a band gap, however, the said band gap is too wide (3 eV) to use the visible light, therefore, a chemical removal of oxygen allows to control such band gap. A common method is to complete a chemical reduction; however, the resulting reduced graphene oxide (rGO) is not soluble in water nor organic solvents. Another parameter to take into consideration, is the lateral size of the graphene-based material which should be less than the thickness of the active layer (~100 nm) in order to be properly used.

Thus, the applied strategy was to reduce the size of the GO after its synthesis, but extremely important is that such process was done without modification of its properties (water solubility, band gap, C/O ratio and functional groups). Afterwards, the smaller size GO is functionalized with octadecylamine (ODA) and chemically reduced (rGO-ODA). This material has an adequate band gap and is now soluble in the common solvents used to prepare the active layer of the OPVs.

However, the rGO-ODA is not suitable for its use in the supercapacitors. The general idea behind this type of device is to be the greenest possible, thus the

preferred solvents cannot be organic solvents. Also, as stated in the introduction, the criteria for a material to be used as electrode for supercapacitors it is the good conductivity and redox activity. In this context it is clear that the GO and rGO are not good candidates for supercapacitors. Thus, the strategy developed was to synthesize a graphene-based material selectively oxidized (SOG). In this case, SOG has the advantage of GO, of being a water-soluble material, but the low oxygen content as in rGO and the high conductivity from graphene.

Finally, the TMDs where synthesized by an exfoliation method. Normally, when a top-down synthesis of TMDs is applied, n-butyl lithium is used. However, due to its toxicity, a new synthesis method with ethanol-water was successfully applied. In order to obtain a graphene in a similar manner than for TMDs, the same method was applied to the graphite nanoparticles, giving as result, the exfoliated graphene (GEX).

In summary, the GO was used as intermediate. The rGO-ODA was applied in the active layer of the OPVs. The SOG, GEX and TMDs were used to make the electrodes of the supercapacitors.

I. Reduced lateral size graphene oxide

It started from graphite nanoparticles (GNPs), using the modified Hummers' method reported previously. (Méndez-Romero et al., 2019) Briefly, 0.5 g of GNPs were oxidized in 30 mL of H_2SO_4 and 0.295 g of KNO_3 with 3 g of $KMnO_4$ to achieve formation of Mn_2O_7 complex. The reaction was carried out for 6 hours, stirring the solution at 450 rpm controlling the temperature below 15 ºC.

The reaction was quenched with 100 mL of DI H_2O and 6 mL of H_2O_2 30%, see Figure 13 a). Next, the obtained bright yellow dispersion (graphite oxide) was centrifuged at 3500 rpm for 10 minutes to remove the supernatant and 100 mL of HCl 10% were added to the precipitate and centrifuged under the same conditions. The washing process was repeated 3 times with DI H_2O.

Afterwards, 80 mL of DI H2O were added, and the dispersion was placed in the ultrasonic bath VWR Symphony Ultrasonic Cleanser Model 97043-944 1 hour for exfoliation, see Figure 13 b). Finally, the supernatant in water dispersion was recovered, stored and labelled as GO-0.

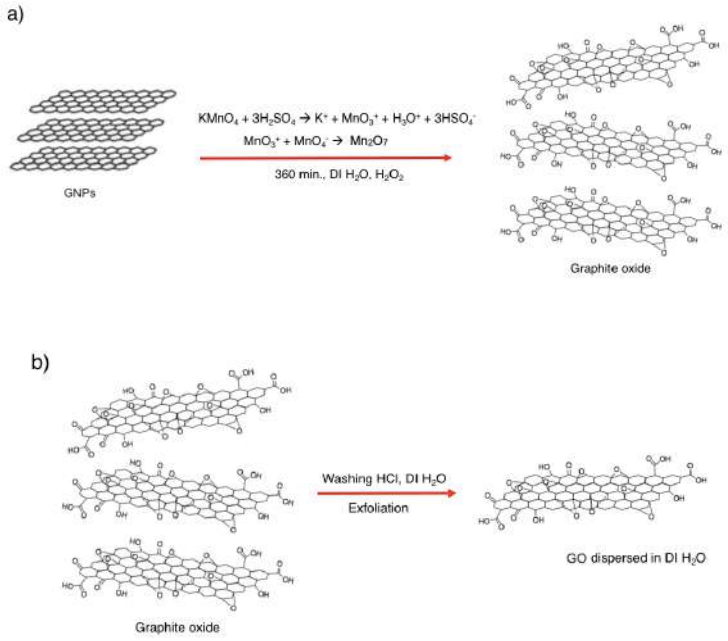

Figure 13. a) Schematic representation of the synthesis of graphite oxide. b) Schematic representation of the synthesis of graphene oxide

The obtained GO aqueous dispersion resulted with an E_g^{opt} of 3 eV. The lateral size decrease of GO was achieved by a Branson sonifier model SFX250, applying a 40% amplitude and a controlled temperature of 18ºC. The procedure was performed as follows: the starting GO dispersion (GO-0) was diluted at [3 mg mL-1] and gauged to 10 mL followed by sonication.

Every 30 minutes for a lapse of 240 minutes, 1 mL of the GO dispersion was taken and gauged at 10 mL in centrifuge vials named as GO-30, GO-60, GO-90, GO-120 and GO-240, referring to the time in the ultrasonic probe. Later, the dispersions were centrifuged at 3500 rpm for 1 hour to remove the less stable GO, then the supernatant was analyzed.

The resulting yield after the size reduction and centrifugation was determinate to be 90%. See a schematic representation in Figure 14.

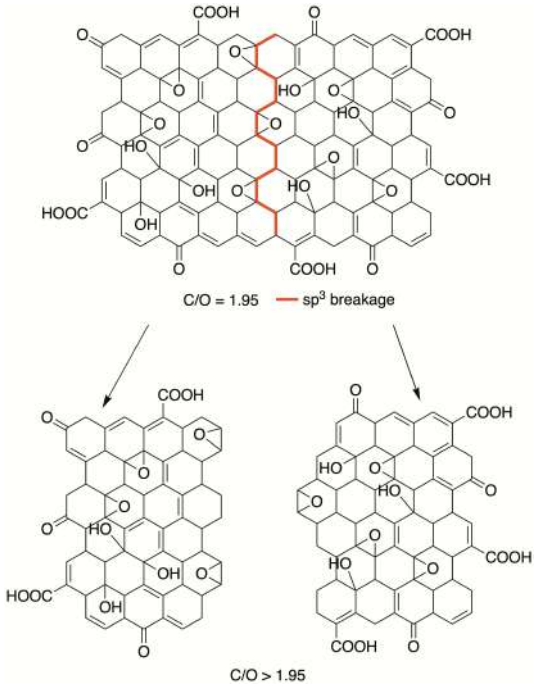

Figure 14. Schematic representation of the size reduction mechanism in the x-y plane, without modification of the C/O ratio.

II. Reduced graphene oxide functionalized by octadecylamine

Starting from the GO, a phase-transfer from water to a desired organic solvent was performed to achieve an electrostatically functionalized GO with octadecylamine (GO-ODA). The functionalization of the fresh synthesized GO dispersed in water, fixed at [10 mg mL^{-1}] to *o*DCB or toluene was performed electrostatically, by mixing a solution of ODA in ethanol [30 mg mL^{-1}] in a 1:1 volume ratio and sonicated for 5 minutes.(Méndez-Romero et al., 2019)

The mixture was stirred at 450 rpm for 5 minutes at room temperature. Subsequently, an equal volume of the desired solvent (*o*DCB or toluene) was added and stirred at 450 rpm for 3 minutes at room temperature, promoting a phase

transfer. The organic phase (GO-ODA) was stored for later use. In Figure 15, it is shown a schematic diagram representing this process.

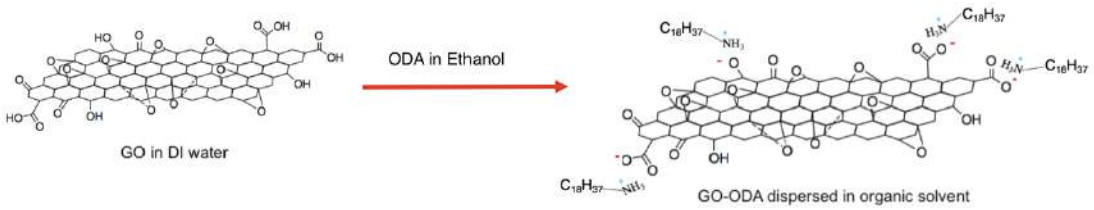

Figure 15. Electrostatic functionalization by ODA.

Finally, the chemical reduction reaction was carried out by adding 100 µL of ascorbic acid-6-palmitate (AA6P) [100 mM] solution in *o*DCB or toluene for each 100 mg of GO, at 98 °C and stirred at 450 rpm for 2 hours. Thus, reduced graphene oxide functionalized with ODA (rGO-ODA) was obtained in solution. The sample was vacuum filtered in a Pall PTFE membrane with a diameter of 47 mm and 0.2 µm pores and dried at room temperature for further characterization

The proposed mechanism of the chemical reduction reaction is described below in Figure 16. In summary, the ascorbic acid-6-palmitate reduces the epoxy groups, while the carboxyl and carbonyl are thermally reduced. Because carboxyl is electrostatically bonded to the amine, the reaction allows a condensation, creating a covalent bonding with water as a by-product, which eventually evaporates from the reaction media. (Méndez-Romero et al., 2019)

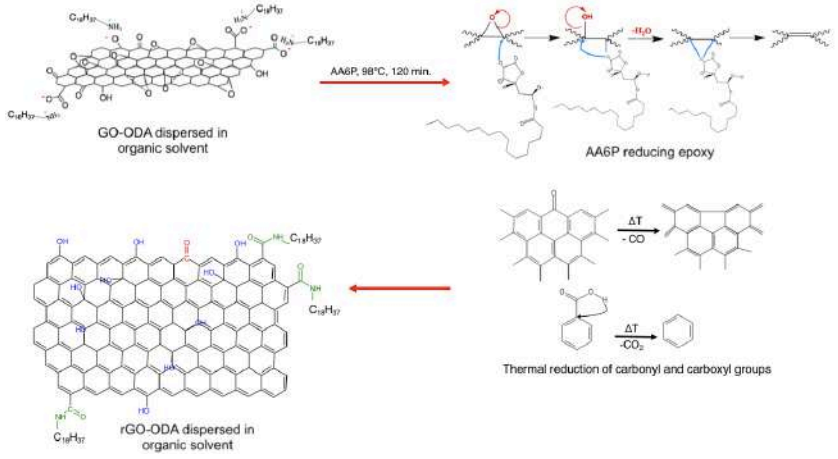

Figure 16. Proposed mechanism for the chemical reduction. (Méndez-Romero et al., 2019)

III. Selectively oxidized graphene

First, 30 mL of a solution of concentrated H_2SO_4 and 0.295 g of KNO_3 were added to a 0.5 g of GNPs. Then 0.3 g of $KMnO_4$ was slowly added to the mixture while using a water bath at 14 °C. This amount of $KMnO_4$ is a tenth from the common ratio 6:1 ($KMnO_4$: graphite)(Méndez-Romero et al., 2019).

Subsequently, the reaction was allowed for 30 minutes in the water bath, which means that the reaction time was decreased twelve times, compared with our previous work (6 hrs.)(Méndez-Romero et al., 2019). Afterwards, the mixture was centrifugated at 4500 rpm for 10 min. Then the supernatant was discarded, and the precipitate was washed with 10% HCl followed by another centrifuge washing steps (3 times) with DI water.

The obtained precipitate was dispersed in DI water using an ultrasonic bath for one hour. Figure 17 shows a schematic representation of the whole process.

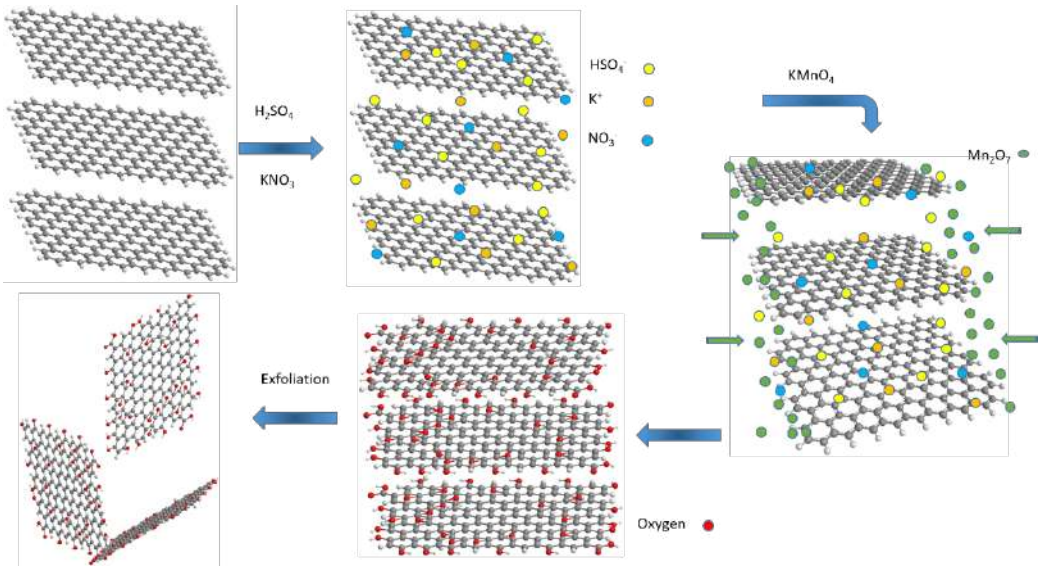

Figure 17. Proposed selectively oxidation mechanism of SOG.

IV. Graphene Exfoliated (GEX), MoS_2 and $MoSe_2$

Here a simple but extremely efficient top-down synthesis approach by liquid-phase exfoliation using ultrasonic probe is applied. First, 20 mL of a solution of

ethanol-water in a 1:1 ratio was added into a vial containing 200 mg of the desired 2D starting material. Then the vial was placed into a water bath at 14 °C for 10 minutes. Afterwards, the ultrasonic probe was placed into the vial with the following parameters: 40% amplitude, on-off intervals of 10 and 1 seconds, respectively for 2 hours, *i.e.*, 30 kJ of applied energy and controlling the temperature of the system to don't be higher than 14 ºC. Then the obtained dispersion was centrifuged at 1000 rpm for 10 minutes with the same acceleration and deacceleration. The precipitate was discarded. Figure 18 shows a schematic for the process.

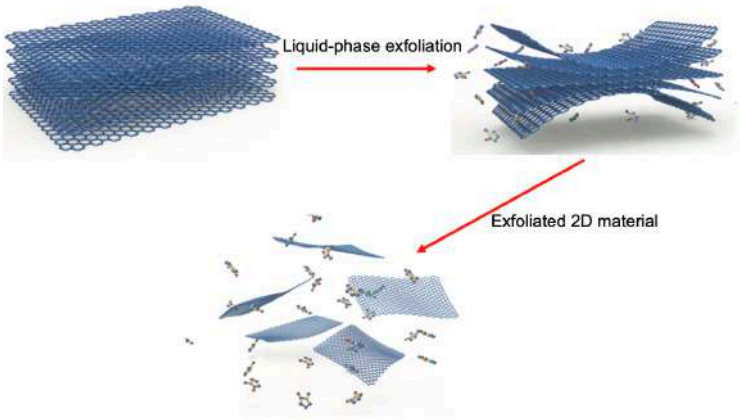

Figure 18. Schematic of the liquid-phase exfoliation. (Wang et al., 2017)

V. Semiconductor polymer poly[4-(5-(4,8-bis(4-chloro-5-(tripropylsilyl)thiophen-2-yl)-6-methylbenzo[1,2-*b*:4,5-*b'*]dithiophen-2-yl)-4-octylthiophen-2-yl)-5,6-difluoro-7-(5-methyl-4-octylthiophen-2-yl)benzo[*c*][1,2,5]thiadiazole]

A new conjugated D-A polymer poly[4-(5-(4,8-bis(4-chloro-5-(tripropylsilyl)thiophen-2-yl)-6-methylbenzo[1,2-*b*:4,5-*b'*]dithiophen-2-yl)-4-octylthiophen-2-yl)-5,6-difluoro-7-(5-methyl-4-octylthiophen-2-yl)benzo[*c*][1,2,5] thiadiazole] was developed. The literature suggests (Subbiah et al., 2015) that the electron-deficient benzo[c][1,2,5]thiadiazole (BT) derivatives (see structure in Figure 19) are promising building blocks to prepare efficient polymeric donor materials for solar cell applications. (Fan, Liu, et al., 2020) The broad absorption in the entire

visible part of the solar spectrum and the relatively high PCE achieved for BT-based polymers have pushed researchers to tune the photo-physical properties of BT-based polymers.(Subbiah et al., 2015)

As previously stated in the introduction, the addition of halogen atoms, contributes to a higher performance, thus, a fluorinated compound was selected.(Fan et al., 2019) Consequently, it was chosen 5,6-difluoro-4,7-bis(4-octylthiophen-2-yl)benzo[c][1,2,5]thiadiazole (DFBT) as an electron accepting unit (see structure in Figure 19) to prepare the new D-A polymer, which is commercially available.(Kini et al., 2017; Subbiah et al., 2015)

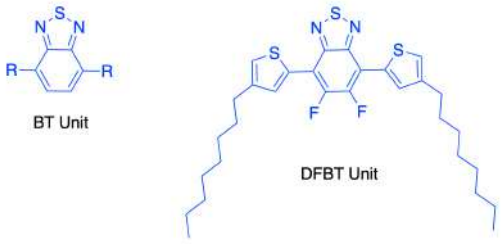

Figure 19. Benzothiadiazole (BT) structures.

On the other hand, the rigid and planar structured benzo[1,2-b:4,5-b′]dithiophene (BDT) is an efficient electron rich unit (see structure in Figure 20) used to prepare high energy converting D–A polymers. In this case, the halogenation strategy was also applied, and silicon heteroatoms were chosen because it was found that significantly affect the crystallinity, extinction coefficient, electron mobility of the polymer acceptors, the morphology and the mechanical robustness of related active layers.(Fan, Su, et al., 2020)

The synthesized donor monomer was ((2,6-bis(trimethylstannyl)benzo[1,2-b:4,5-b']dithiophene-4,8-diyl)bis(3-chlorothiophene-5,2-diyl))bis(tripropylsilane), from here called UMM, see Figure 20.

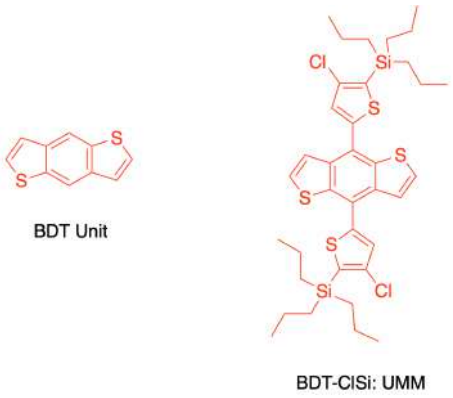

Figure 20. Benzodithiophene (BDT) structures.

Finally, the Stille copolymerization between UM6 and DFBT using the standard procedure. Briefly, using 1 equivalent of UM6 and DFBT (2mmol) and 0.05 equivalents of $Pd(PPh_3)_4$ as catalyst, see Figure 21. After 25 hours, the reaction was quenched with methanol and dissolved in chloroform for purification by wet silica column to finally filtrate it and vacuum dried it, resulting in the new polymer PUM2 with 40% yield.

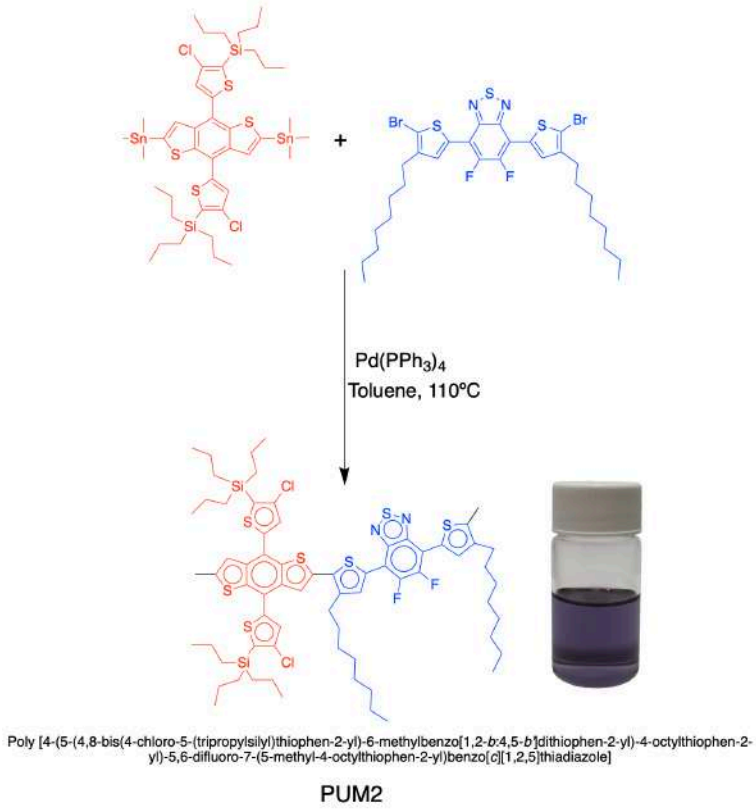

Figure 21. Stille copolymerization for PUM2 and a digital picture of 0.01 mg mL^{-1} in chloroform.

VI. Organic Solar Cells

The architecture applied for the organic solar cell was similar as the one presented in Figure 8. However, for better clarity, the applied geometry in this work is shown in Figure 22.

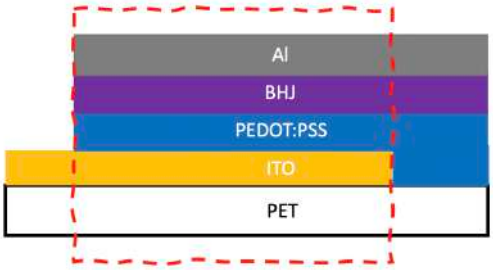

Figure 22. Organic solar cell architecture.

Four types of devices were done, named as D1, D2, D3 and D4. The difference between them was the active layer composition, see Table 1. The BHJ dispersion was done as follows: first, the semiconducting polymer was dissolved in chloroform at 10 mg mL^{-1}, second the acceptor material was also dissolved in the same conditions. Finally, both were mixed and stirred at 450 rpm for 30 minutes.

Table 1. Organic solar cell devices

Device	Donor	Acceptor	Ratio
D1	P3HT	$PC_{61}BM$	1:1
D2	P3HT	rGO-ODA	1:1
D3	PUM2	rGO-ODA	1:1
D4	PUM2	$PC_{61}BM$	1:1

The selection of such nanocomposites is explained as follows: D1 is the most common solar cell and the PCE its well-known (here used as a reference sample), the D2 replaces the $PC_{61}BM$ for rGO-ODA to see the feasibility of its use as an acceptor. The D3 is the proof of concept where the two new synthesized materials

in this thesis can work as a donor and as an acceptor. The D4 is intended to analyze the feasibility of the PUM2 with commercial $PC_{61}BM$ and compare it with D1 and D3.

The devices were made on PET substrates (2x3 cm) covered with ITO (120 Ω/square), purchased from Sigma Aldrich. First, a 0.5 cm from the larger side of the substrate was kept by 5 seconds into a 1:1:5 solution of HCl, HNO_3 and H_2O at 80ºC in order to remove the ITO, as seen in Figure 22. Immediately, the acid solution was rinsed with DI water. Afterwards, a cleaning procedure in the ultrasonic bath with DI water, isopropanol and ethanol was carried out. Then, the clean substrates were treated with H_2O_2 (30% vol) at 80ºC for 30 min. Prior to use the substrates, were rinsed with DI water.

The poly(3,4-ethylenedioxythiophene) polystyrene sulfonate (PEDOT-PSS) and the active layer were deposited by spin coating. First, 150 μL of PEDOT-PSS were spin coated at 3500 rpm by 15 s and then at 5000 rpm for 30 s. Next, a thermal annealing was carried out at 100ºC by 30 minutes. Then, a solution of the different BHJs was deposited by spin coating (200 μL) at 1500 rpm for 15 s and then 2500 rpm for 30 s. Finally, an electrode of 60 nm of Al was deposited by sputtering.

VII. Supercapacitors

The architecture used to develop the supercapacitors was the Swagelok cell, seen Figure 23.

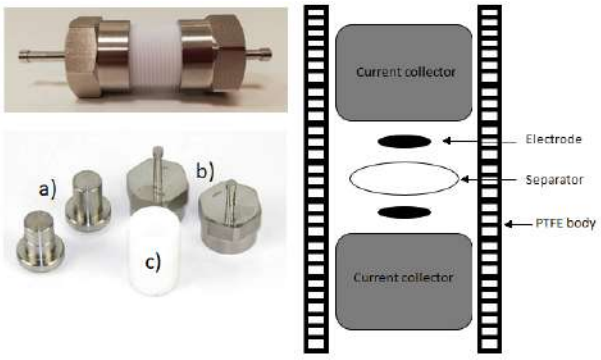

Figure 23. Swagelok cell and assembly of its components: a) current collector, b) Swagelok firring part, c) PTFE body

The supercapacitors were done with GEX, MoS_2 and SOG. Seven different devices were fabricated, Table 2 shows the difference between them.

Table 2. Electrodes for fabricated supercapacitors

Device	Composition	Active material (mg cm^{-2})	Ratio
S1	GEX	2.61	1
S2	MoS_2	2.61	1
S3	SOG	0.22	1
S4	GEX-MoS_2	2.61	1:1
S5	GEX-MoS_2	1.3	1:1
S6	GEX-MoS_2-SOG	2.61	1:1:1
S7	GEX-MoS_2-SOG	1.3	1:1:1

The selection of such electrodes is explained as follows: Devices S1, S2 and S3 were conceived to analyze the feasibility of the 2D materials. The S4 and S5 were developed in order to analyze if there was an improvement in the capacitance or capacitance retention at high scan rates by a synergistic effect between the GEX and MoS_2 nanocomposite electrode. Also, the different amount of active material helped to understand if there is a relationship to the gravimetric capacitance. Finally, the devices S6 and S7 were developed to analyze the advantage of a ternary system and also the relation to the gravimetric capacitance.

The supercapacitors were fabricated as follows: All the materials were processed from dispersion in water-ethanol, they were poured on top of a 3.5 cm diameter polytetrafluoroethylene (PTFE) membrane (0.45 μm pore size) and filtrated under vacuum and pressed manually to prepare a film using 100 μm spacers to set the thickness. To obtain supported electrodes, SOG, and 2D materials nanocomposite membranes were cut into circles of 8 mm diameter using a hollow hole press.

Once the electrodes were made, a Swagelok cell was used to fabricate the devices. The assembly consisted of placing the active area of the electrode over the current collector. Next, a 12 mm diameter fiberglass (separator) was placed on top of the support area of the electrode. Then, 50 µL of 1M Na_2SO_4 was added over the separator. Subsequently, the support area of the second electrode was positioned in alignment with the first one over the separator, and the bottom part of the current collector was coupled with the Swagelok fitting part. Finally, the PTFE body matched around the current collector, and the remaining components were fitted accordingly with a soft scroll to seal the cell. The device was connected by clamps to start electrochemical measurements with Gamry series 1010E Series potentiostat.

Results and Discussion

In order to assess the synthesized materials and the fabricated devices, the characterizations will be grouped by technique and by type of material or device. Also, for clarity of the reader it could help to easily compare the results, whom should be familiarized by now with the terms and materials; however, a short summary is presented.

Chemical and structural studies

The synthetized graphene-based materials (GBMs) were 4: small lateral size graphene oxide, reduced graphene oxide functionalized with ODA (rGO-ODA), selectively oxidized graphene (SOG) and graphene exfoliated (GEX). Two different transition metal dichalcogenides were studied: MoS_2 and $MoSe_2$. One conjugated polymer was synthesized (PUM2). Solar cells and supercapacitors were fabricated.

First the 2D materials will be analyzed by X-ray Photoelectron Spectroscopy (XPS) using a Thermo Scientific Escalab 250Xi instrument, in order to understand the chemical behavior and modifications of the synthesized materials at its surface; all the samples were vacuum dried and analyzed in powder form. Then, Raman spectroscopy studies were performed to analyze the degree of crystallinity of the GBMs as well as the number of layers of the TMDs, this characterization was done with a confocal Raman microscope alpha300R from WITec with 50x objective was used for all measurements and the system was used unpolarized with a 532 nm laser. The laser power was reduced to avoid sample damage. All spectra were gathered over 2 s exposures and 10 accumulations. A drop casting sample was prepared from the 2D materials dispersion on a glass slide. Finally, X-Ray Diffraction (XRD) Panalytical Empyrean diffractometer, was used in order to analyze the interplanar distance in the synthesized 2D materials.

In order to confirm the chemical composition and the structure of the synthesized polymer included XPS and Nuclear Magnetic Resonance Spectroscopy

(NMR), ^{1}H-NMR spectrum was recorded on an automated Varian Inova 400 MHz NMR spectrometer. Chemical shifts are given in δ (ppm) relative to the tetramethylsilane (TMS). Deuterated chloroform $CDCl_3$ (1H: 7.26) was used as solvent.

Optoelectronic studies

In order to investigate the viability of the synthesized materials to be used as the active layer in a solar cell, the absorption spectrum was analyzed by UV-Vis spectroscopy, as well as the optical band gap. All the materials were dispersed and diluted to 0.01 mg mL^{-1} and were analyzed by a UV-Vis-NIR Spectrometer Perkin Elmer instruments Lambda 900. The cyclic voltammetry (CV) performed with an Electrochemical Workstation CH-Instruments 650A and with a Keithely 2430 sourcemeter with a 4-wire configuration were used to obtain the HOMO-LUMO energy levels and therefore the electrical band gap. The CV measurements were done under N_2 atmosphere using a three-electrode setup. The first two electrodes were Pt wires (referred as working electrode and counter electrode) and the third one was the reference electrode comprising an Ag wire in 0.1 M $AgNO_3$ aqueous solution. A 0.1 M solution of tetrabutylammonium hexafluorophosphate ($TBAPF_6$) in anhydrous acetonitrile was used as the electrolyte. The electrolyte was bubbled with N_2 gas prior to each measurement to remove any oxygen residues. The working electrode was coated with the materials films by drop casting a 10 mg mL^{-1} dispersion onto the Pt wire. The forward (oxidation) and reverse (reduction) scans were measured separately on pristine films at a scan rate of 50 mV s^{-1}, with a minimum of three independent scans for each sample. The reference electrode was calibrated versus the ferrocene/ferrocenium (Fc/Fc^{+}) redox couple at the end of the measurements.

Device characterization

The solar cells were characterized with a Keithely 2430 sourcemeter with a 4-wire configuration. Supercapacitors measurements were conducted with a Gamry Reference 1010E series.

I. XPS of Graphene-Based Materials

The XPS is an extraordinary technique to analyze the graphene-based materials (GBMs), since it provides an insight of the different atoms bonded to the carbon. All the GBMs used in this thesis presented 3 representative signals in the high resolution C1s spectra recorded from 279 eV to 298 eV.: C-C, C-O and C=O at 284.48 eV, 286.88 eV and 288.88 eV, respectively. (Méndez-Romero et al., 2019; Velasco-Soto et al., 2015)

To easily understand the changes during the different chemical modifications, the starting graphitic material is also included, the reader can recall from the methodology that it was graphite nanoparticles (GNPs). The C1s core level spectra are shown in Figure 24, where Figure 24 a) corresponds to GNPs and Figure 24 b) to GO. The signal coming from the GNPs is composed only by C-C, with a single contribution at 284.48 eV, the absence of any other signal, reveals purity and crystallinity of the material, proving at the same time information that no previous oxidation is present. After the Hummer's method, the obtained GO shows a completely different spectra, in agreement with a highly oxidized material. (Méndez-Romero et al., 2019; Velasco-Soto et al., 2015)

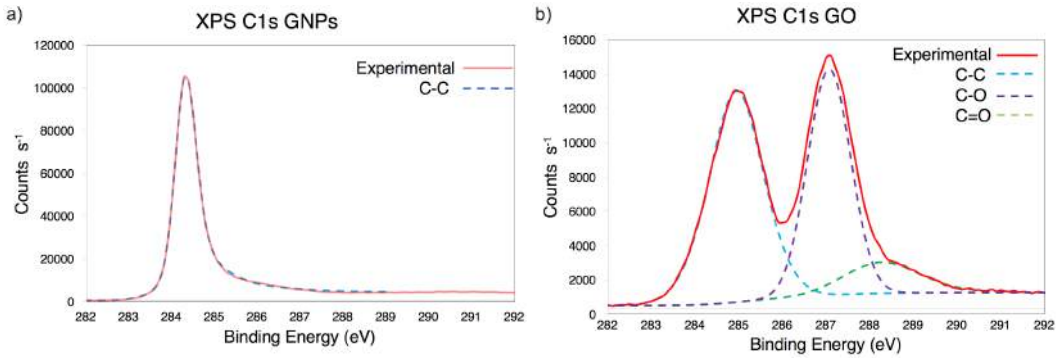

Figure 24. High resolution XPS C1s analysis of a) GNPs and b) GO

The next modification done was a lateral size reduction. It was previously stated that the materials intended to be use as active layers should have a smaller size than the thickness of the layer itself (Uddin & Yang, 2014). Interestingly, the lateral size decreases without compromising other relevant parameters, such as C/O

ratio, crystallinity and band gap. It was described in the methodology section that the process involved sonification through time of GO. Thus, GO-0 corresponds a GO without treatment, GO-30 corresponds a material that was kept for 30 minutes in the ultrasonic probe, and so on. The lateral size reduction for the GOs showed a small difference (less than 3%) in the C/O ratio as seen in Figure 25.

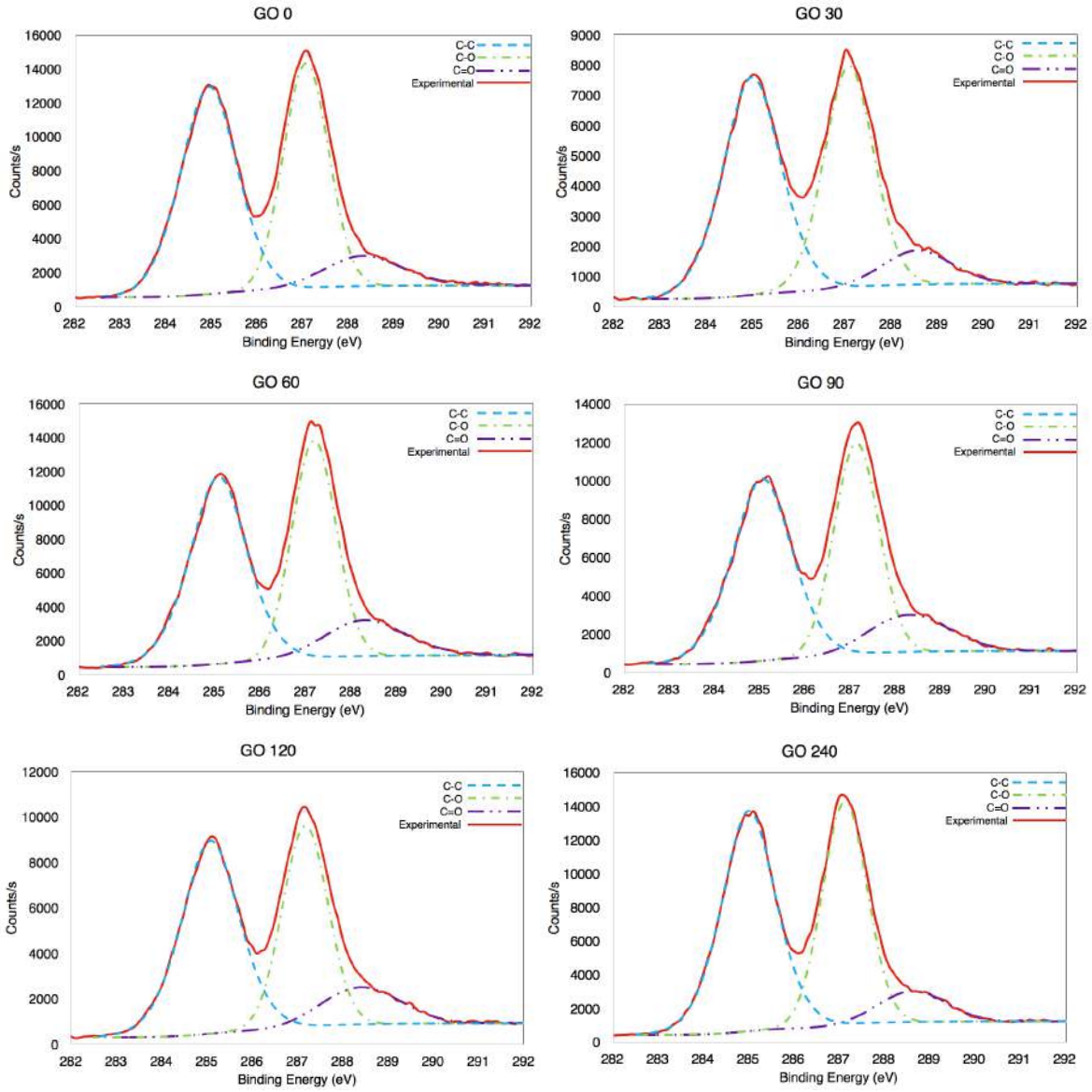

Figure 25. High resolution XPS C1s analysis of GOs after 0, 30, 60, 90, 120 and 240 minutes of sonication.

In order to analyze the relation between lateral size against the applied energy during sonication, the plot in Figure 26 shows the progression in size reduction

depending on the energy during the time of the experiment. It is clear that the major change in size is achieved during the first stage of the experiment (first two hours), however, based on the plot one can interpolate or extrapolate the required energy in order to obtain a specific desired size. This plateau behavior could be explained by the depletion of sp^3 breakage areas, confirming that the mechanism is related to the lowest bond dissociation energy (BDE) by mechanical vibration, see more details in annexed ***Paper V***.

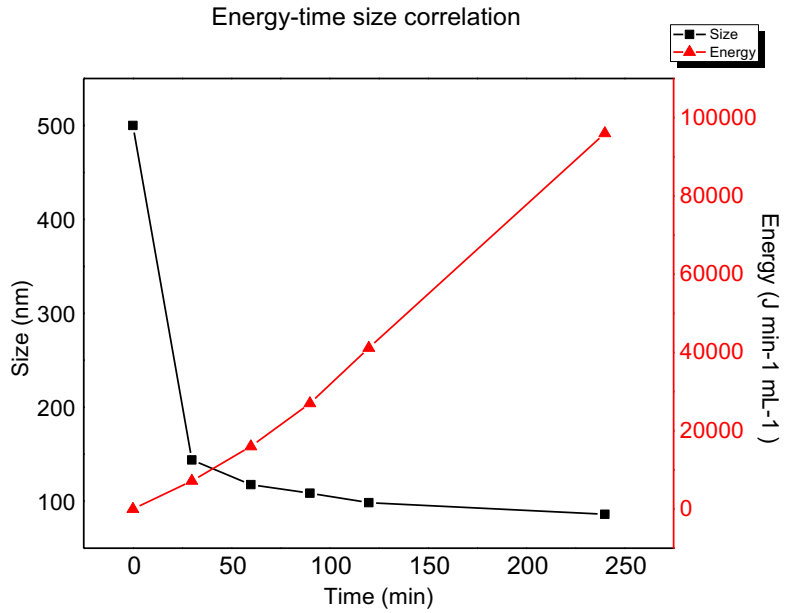

Figure 26. Lateral size obtained by Dynamic Light Scattering versus applied energy during sonication.

As can be noticed, the XPS results were divided in 3 groups, Figures 24, 25 and 27. The first group are the starting material and the intermediate (GO), the second group, Figure 25 shows the modification of the intermediate and the third group of materials, in Figure 27 it is shown the high resolution C1s from GEX, SOG and rGO-ODA which are the final products, that were applied in the fabrication of devices. As one can see, the spectra obtained from GEX is very similar to the starting GNPs, with just a small amount of carbonyl (<1%). Deconvoluted peaks of the SOG in Figure 27 b) show the presence of oxygen functional groups due to the oxidation reaction. It is clear that even when the oxidation takes place under mild conditions

and just 30 minutes it is enough to introduce oxygen functionalities into the structure. The signal coming from rGO-ODA in Figure 27 c) is characteristic of a highly reduced state, presenting a very small contribution of C-O at 288.08 eV and a new signal related to C-N at 285.48 eV, suggesting a covalent functionalization by ODA.(Méndez-Romero et al., 2019)

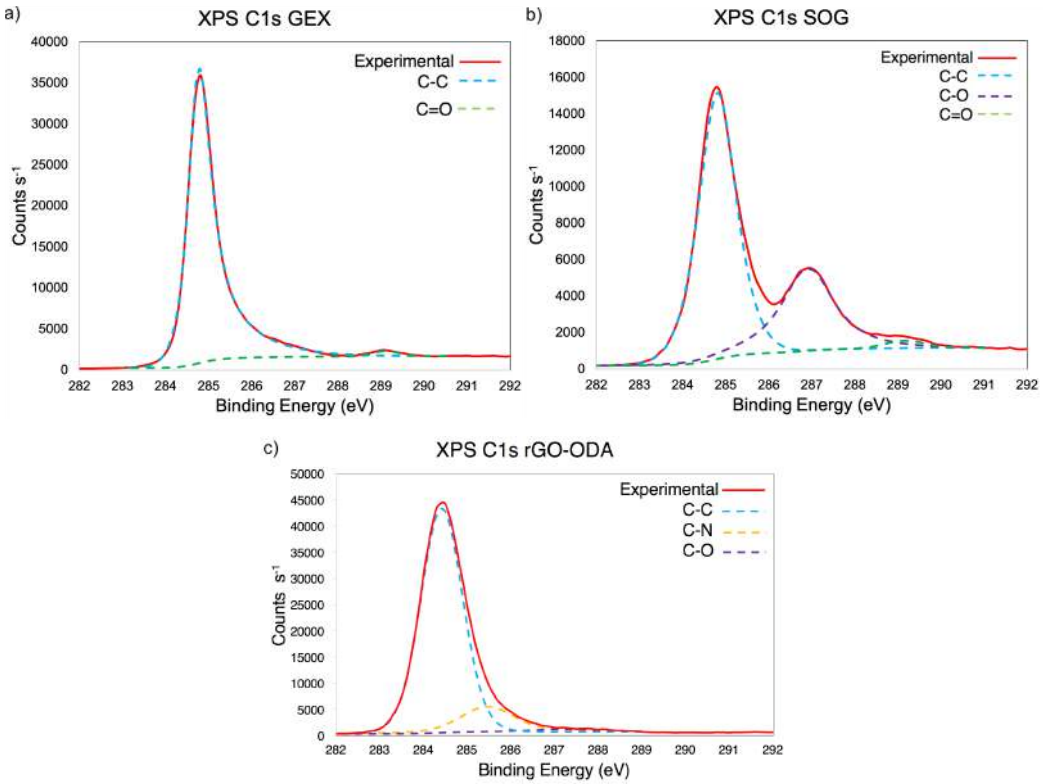

Figure 27. High resolution XPS C1s analysis. a) GEX, b) SOG and c) rGO-ODA.

In Table 3, the C/O ratio from all the GBMs is presented. It is clear that one of the main advantages of this type of materials, is the capability to tailor the oxygen content and therefore its properties: optical band gap, HOMO-LUMO energy levels, solubility and further functionalization. The GBMs are extremely diverse and in Table 3 it is clear that they were successfully modulated in the most important parameter, besides the size.

Table 3. C/O ratio for the Graphene-Based Materials

Material	C/O ratio	Solubility
GNPs	∞	None
GO	1.95	H_2O
GEX	199	H_2O:CH_3OH
SOG	3.48	H_2O
rGO-ODA	99.77	$CHCl_3$

It is important to mention that these values are very interesting. Of course, the results from the GNPs and GO are expected and previously reported. (Hou et al., 2018; Vallés et al., 2016) However, a previous report from our research group found a C/O ratio of 3.25 for its highest reduced GO (Velasco-Soto et al., 2015), which is even more oxidized than the synthesized SOG, proving the advantage of this new material. Because this new material does not required a reduction process to achieve the said oxidation degree and more importantly, keeping a good solubility in water, conversely to the reported rGO (Velasco-Soto et al., 2015). It is clear that the rGO-ODA is a highly reduced material, even when compared with an rGO annealed at 1000ºC (Vallés et al., 2016). In the case of the GEX, the C/O ratio is comparable to the graphene obtained by chemical vapor deposition (CVD)(Brownson et al., 2014), which is remarkable.

II. XPS of TMDs

For the MoS_2, the Mo 3d level spectra were recorded from 222 eV to 240 eV and is shown in the Figure 28. In this case, one can clearly see that before and after the synthesis process, the contributions from the Mo^{4+} $3d_{5/2}$ and Mo^{4+} $3d_{3/2}$ were not affected indicating that material is not oxidized and also the crystalline phase 2H is not modified. This is something that need to be highlighted, since one could expect some oxidation, since the synthesis is done in an aqueous media; however, this result shows the excellent control during the process, avoiding the undesired

oxidation. As expected, the signal for S2s at ~226.2 eV is present. The minor contribution from Mo^{6+} $3d_{5/2}$ and Mo^{6+} $3d_{3/2}$ at ~233 eV and ~235.4 eV, respectively, is consistent with a minor oxidation but present from the initial sample without further modification.(Truong et al., 2017)

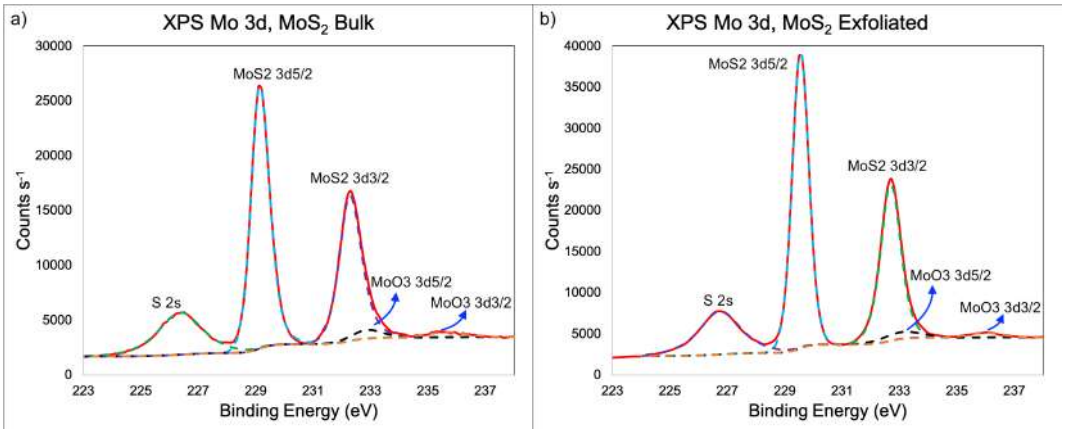

Figure 28. High resolution XPS spectra for the Mo 3d region of the a) MoS_2 starting material and b) MoS_2 after the exfoliation.

For the $MoSe_2$, the Mo 3d level spectra were also recorded from 222 eV to 240 eV as shown in the Figure 29. In this case it is fascinating to point out that the spectra are similar, but the exfoliated sample does not present the oxidation contribution from Mo^{6+} $3d_{5/2}$ and Mo^{6+} $3d_{3/2}$ at ~233 eV and ~235.4 eV, respectively. This is an indication that the exfoliation process does not oxidize the material, conversely though, it was beneficial by removing the pre-existing oxidation.(Truong et al., 2017)

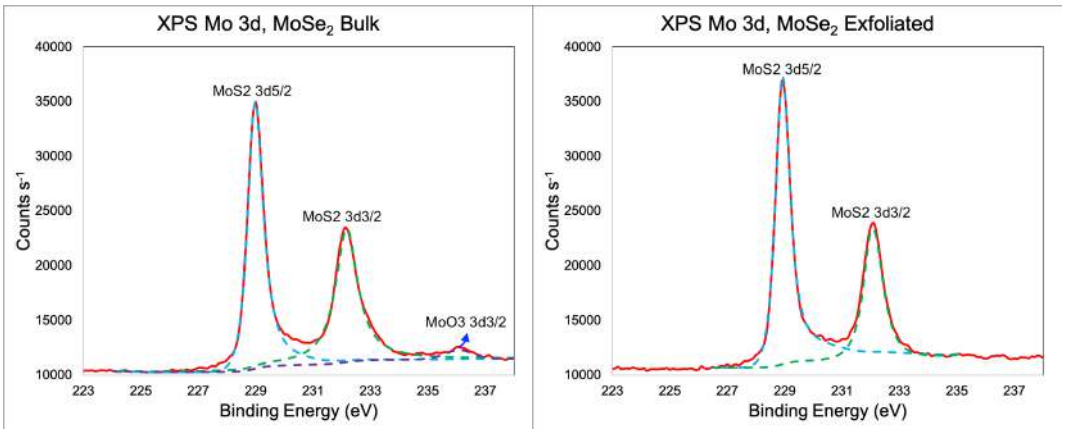

Figure 29. High resolution XPS spectra for the Mo 3d region of the a) $MoSe_2$ starting material and b) $MoSe_2$ after the exfoliation.

In the case of the synthesis of TMDs, one could summarize that the process did not affect the crystalline structure and the chemical composition, while it allowed to have an aqueous media dispersion.

III. Raman Graphene-Based Materials

In order to compare the structural quality of the graphene-based materials, Raman spectra (Figure 30) recorded with 2.33 eV laser energy is presented. It is well known that the particular dispersion of π electrons in graphene offers a powerful and efficient insights of their electronic properties, and therefore of its crystallinity. It can be noticed that all spectra exhibit an intense band from 1450-1660 cm^{-1} corresponding to the *G* band due to vibrational E_{2g} degenerative mode observed in sp^2 carbons. Furthermore, another band is observed at 1260-1400 cm^{-1}, assigned to the *D* band and related to the A_{1g} mode. The *D* peak is originated due to the interaction between phonons and defects, such as in-plane substitution heteroatoms, vacancies, or grain boundaries.(M. Dresselhaus et al., 2010; M. S. Dresselhaus et al., 2010; Ferrari, 2007)

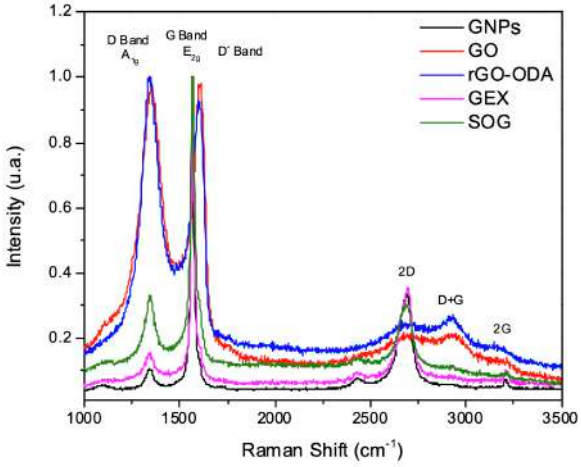

Figure 30. Raman Graphene-Based Materials

For better clarity, the section between 1200 to 1700 cm^{-1} is presented in the Figure 31. In this regard, previous studies (Boran & Gürer, 2019; Wang et al., 2020) used *D* peak to quantify the number of defects in graphene by means of the intensity (peak integrated area) ratio of *D* and *G* peaks (I_D/I_G).

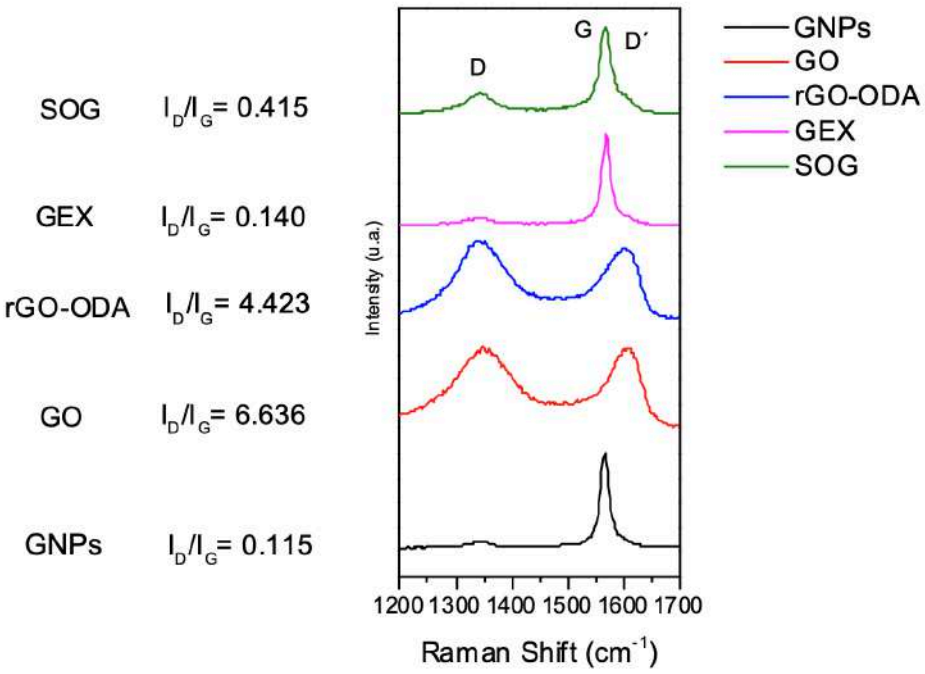

Figure 31. Crystallinity of Graphene-Based Materials by Raman.

As expected, the material with the best crystallinity are the starting GNPs, since they were not subjected to any process. The GO has the lowest crystallinity but interestingly, the rGO-ODA does not recover the crystallinity, despite the highly chemical reduction shown in the XPS results. It is worth to point out, that the I_D/I_G value for SOG is almost 16 times lower than GO and 47 times lower when compared to the GEX. These results indicate that GEX and SOG exhibit crystallinity that is more related to graphene grown by CVD (Brownson et al., 2014; Li, Guo, et al., 2017; Li, Smith, et al., 2017) rather than GO or rGO, which is excellent taking into account the simplicity of the method and its scalability.

IV. Raman of TMDs

Raman characterization of TMDs allows to stablish the number of layers present in the synthesized materials. This is important since the number of layers in the TMDs are directly related to its band gap. Bulk MoS_2 is known to have an indirect

band gap of 1.2 eV, 3L- MoS_2 has 1.35 eV band gap, 2L- MoS_2 has 1.65 and 1L-MoS_2 has 1.8 eV. (Lee et al., 2012)

Raman spectra of MoS_2 is shown in Figure 32. The frequency difference ($\Delta\omega$) between out-of-plane (A_{1g}, ~404 cm^{-1}) and in-plane (E^1_{2g}, ~385 cm^{-1}) phonon modes in the Raman spectra depends on the number of layers of MoS_2 in the case of less than 10 monolayers and increases with an increase in the number of layers. The frequency differences of the two modes are ~19.2 cm^{-1}in 1L- MoS_2, ~22.3 cm^{-1} in 2L-MoS_2, and 24.4 cm^{-1} in 3L MoS_2. (Mouri et al., 2013)

In the particular case of the synthesized MoS_2, a $\Delta\omega$ of 22.5 cm^{-1} of the vibrational E^1_{2g} mode and the A_{1g} mode observed between 360-420 cm^{-1} is related to a two-layers system, as seen in Figure 32.(Mouri et al., 2013)

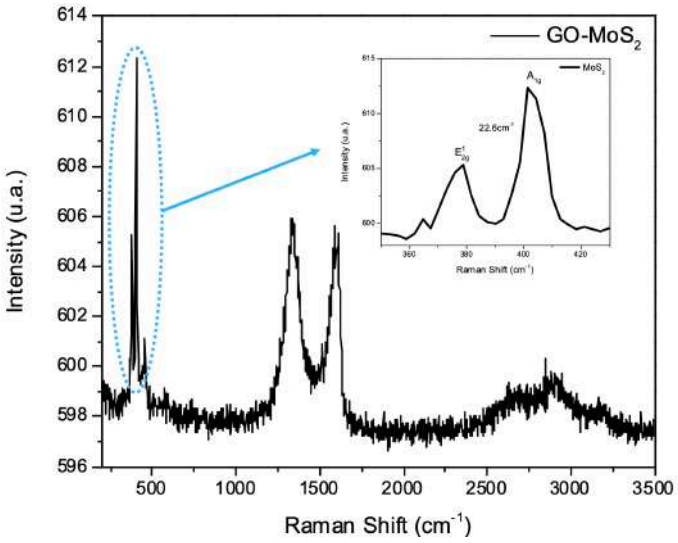

Figure 32. Raman spectra from the synthesized MoS_2. The inset is a zoom in of the frequency difference ($\Delta\omega$) between out-of-plane (A_{1g}, ~404 cm^{-1}) and in-plane (E^1_{2g}, ~385 cm^{-1}) phonon modes.

In the case of the $MoSe_2$, the bulk material is known to have a band gap of 0.84 eV, while the single layer is around 1.34 eV. (Tongay et al., 2012) The Raman analysis from the $MoSe_2$, is different compared with MoS_2. In $MoSe_2$, there are 3 features to take into account, the material has out-of-plane A_{1g}, and in-plane E^1_{2g}, phonon modes but at different Raman shift positions and also the B_{2g} mode, which

is inactive in bulk, but becomes Raman active due to the breakdown of translation symmetry in few layers (2,3,4 and 5 layers). In the single layer the A_{1g} mode it is centered a 241 cm^{-1}, E^1_{2g}, at 287.3 cm^{-1} and the B^1_{2g} at 353 cm^{-1} does not appear. (Tongay et al., 2012; Tonndorf et al., 2013)

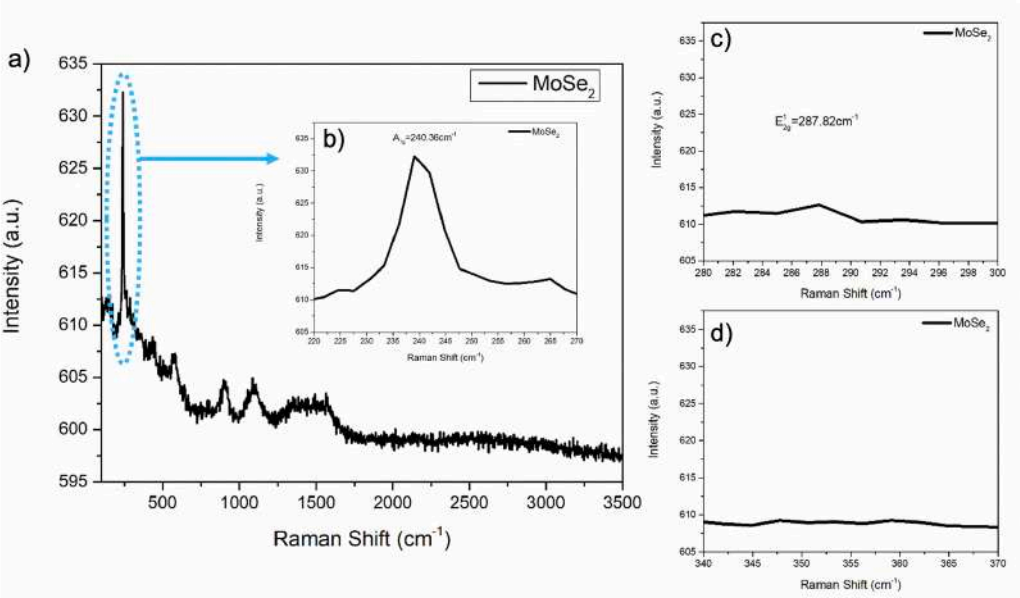

Figure 33. a) Raman spectra from the synthesized $MoSe_2$. b) The zoom in for the out-of-plane A_{1g} mode. c) A zoom in for the in-plane E^1_{2g}, phonon mode. d) Inactive B^1_{2g} mode.

The results presented in Figure 33 shows the main three features in the insets, in Figure 33 b) shows a zoom in the A_{1g} mode at 240.36 cm^{-1}, Figure 33 c) shows the E^1_{2g} mode at 287.82 cm^{-1} and in Figure 33 d) the mode B^1_{2g} at 353 cm^{-1} is inactive, these 3 features are consistent for a single layer material.

In the XPS analysis was already stated that the synthesis process does not affect the chemical composition, and with the Raman study, it is also possible to conclude that the synthesis allowed to obtain a single-layer and two-layers materials.

V. X-Ray Diffraction (XRD)

X-Ray diffractograms are commonly used to measure the interplanar distance in 2D materials trough the Bragg's Law: $n\lambda=2d(\sin\theta)$, where n is an integer, λ is the

wavelength of X-rays, *d* is the distance between the planes of the crystal lattice and, θ is the angle between the incident rays and the scattering planes. In this section, the 2D materials analyzed are the GNPs (for comparison purposes), SOG, GEX and both TMDs. For clarity purposes, the results are divided in four figures.

In Figure 34 for the initial GNPs and for the obtained SOG, it can be seen that GNPs sample has a very sharp peak corresponding to the (002) plane centered around 26.5°, which is widely known from graphite materials and it is related to an interplanar distance of 0.335 nm.(Méndez-Romero et al., 2019) In the case of SOG, the diffractogram exhibit a peak at 26.5°, nevertheless, the peak is lower in intensity and wider. From this result, one can infer the following: first, preserving this peak means that the graphitic structure or conjugated network is maintained, which is in agreement with the aforementioned XPS and Raman results previously showed. Second, the intensity of the peak is proportional to the number of graphene layers stacked suggesting a good exfoliation.

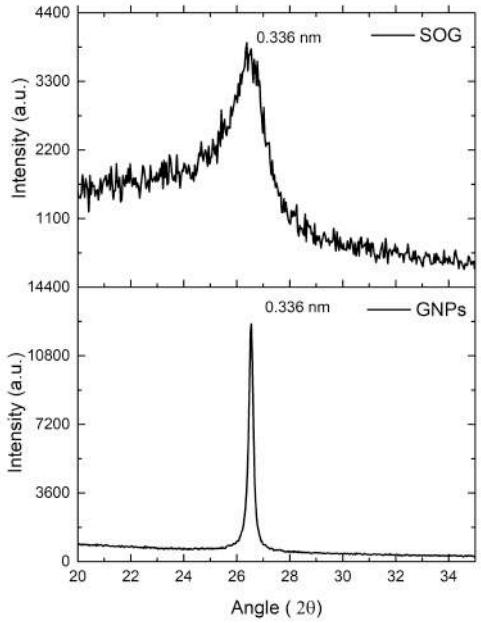

Figure 34. XRD from SOG and GNPs

The comparison between the GEX and GNPs, conversely, do not follow the same behavior than the SOG and GNPs and one could expect that since the XPS

showed almost an identical spectrum between GEX and GNPs. The results showed in Figure 35, suggests a different behavior. The interplanar distance in GEX is larger, in 0.115 nm, meaning that the restacking in GEX is not as high as one could expect, due to Van der Waals interactions.

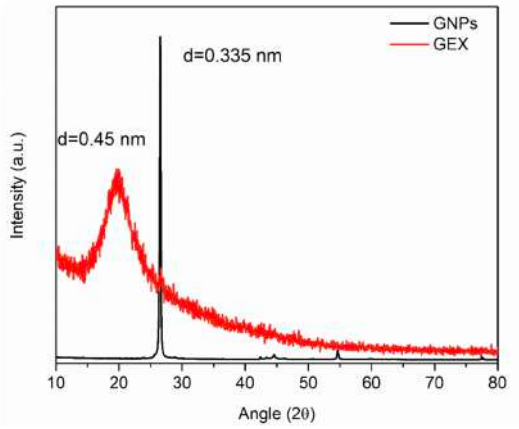

Figure 35. XRD from GEX and GNPs

In the case of the TMDs, MoS_2 in bulk and exfoliated (c.f. Figure 36) have minimal difference (0.004 nm) between the interplanar distance from both samples, revealing a high degree of restacking when the sample is dried.

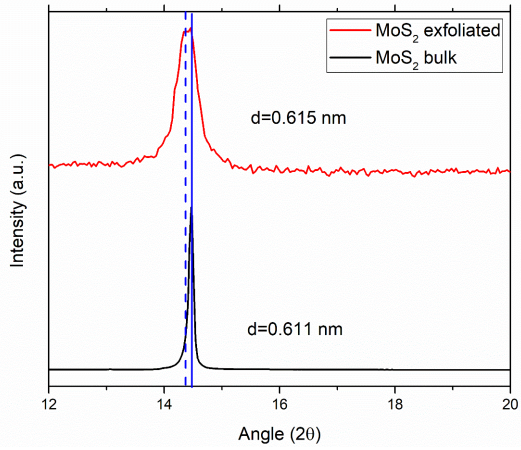

Figure 36. XRD from MoS_2 and MoS_2 exfoliated.

Finally, for $MoSe_2$ shown in Figure 37, the bulk and exfoliated samples have the same shape and both peaks at 13.88º. The difference in the number of layers can be seen in the intensity, which is 4 times smaller in the case of the exfoliated material. However, it shows a high degree of restacking when the sample is dried.

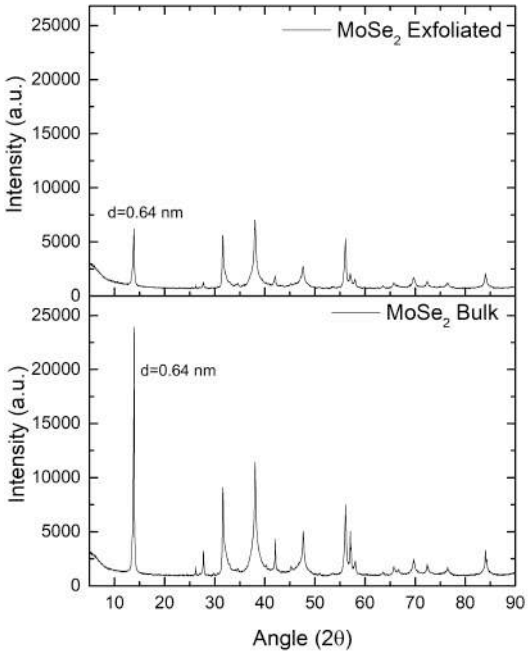

Figure 37. XRD diffractogram from $MoSe_2$ exfoliated and $MoSe_2$ bulk .

There are some important points to note. First, there was not a change in the phase from the synthesized materials, *e.g.,* there are not a 1T phase in the TMDs. Second, this technique probes that the exfoliation process was carried out successfully in all the samples, since the peaks are smaller after the synthesis. Finally, it also shows the high tendency of the 2D materials to be restacked when dried.

VI. XPS and NMR of polymer PUM2

The polymers are usually not analyzed by XPS. However, it was considered as an option because is highly sensitive, straight forward to analyze and fast when compared to NMR (H, and C), MALDI-TOF, among others.

The XPS survey of the polymer can be seen in Figure 38, the data acquired from it, matches with the structure of the polymer poly[4-(5-(4,8-bis(4-chloro-5-(tripropylsilyl)thiophen-2-yl)-6-methylbenzo[1,2-*b*:4,5-*b'*]dithiophen-2-yl)-4-octylthiophen-2-yl)-5,6-difluoro-7-(5-methyl-4-octylthiophen-2-

yl)benzo[*c*][1,2,5]thiadiazole] with a condensed formula: $C_{68}H_{88}Cl_2F_2N_2S_7Si_2$, which is a good approximation from the values acquired from XPS, taking into consideration that hydrogen is not detected: C1s 79.26%, S2p 8.32%, N1s 3.67%, Cl2p 3.29%, F1s 2.76% and Si2p 2.69%.

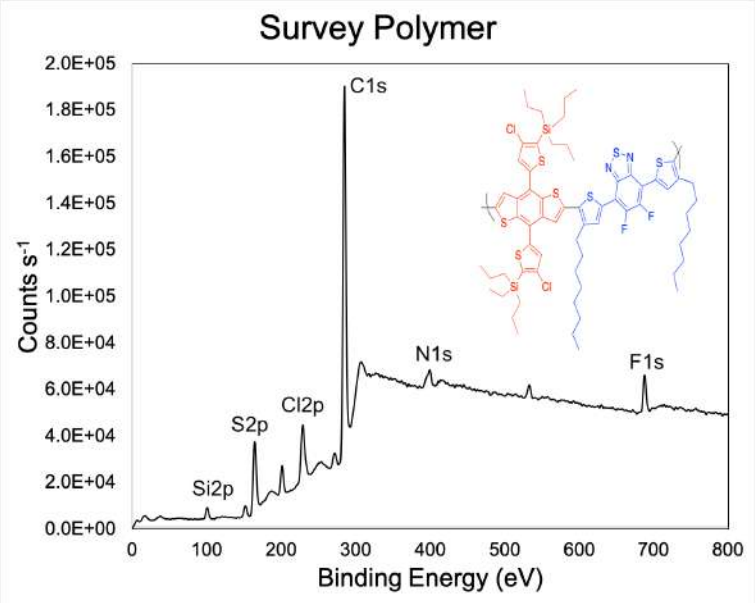

Figure 38. XPS survey from polymer PUM2.

Nuclear magnetic resonance spectroscopy, commonly referred to as NMR, has become a dominant technique for determining the structure of organic compounds. The most simplistic way to describe NMR, is similar than XPS: in XPS, the bonding energy between atoms is measured and it will be different depending on the atoms and the type of bond (single, double, etc.). Thus, it is possible to determine the type of bonded atoms; in the case of proton NMR, the samples are irradiated with a magnetic field at certain frequency. Since electrons are charged particles, they move in response to the external magnetic field (B_o) so it generates a secondary field that opposes the stronger applied field. This secondary field shields the nucleus from the applied field, so B_o must be increased in order to achieve resonance (absorption of radiofrequency energy). Most organic compounds exhibit proton resonances that fall within a 12 ppm range. In this range, the signal from protons bonded to different groups appear, for example, protons from carboxylic

acids, appear between 10 to 12 ppm, the aromatics between 6 to 8, alkanes between 0 and 2, etc.(Murto et al., 2018)

The analysis of the NMR spectra is usually complex; nevertheless, it is possible to simulate it and compare it with the experimental result, making simpler its analysis. In Figure 39, the simulated and the experimental proton NMR are presented, as can be noticed, they are very similar, probing the correct structure. The list of chemical shifts (δ) ^{1}H NMR signals at 400 MHz frequency in $CDCl_3$ are presented, in parenthesis is written the type of signal and the number of protons it represents. The signals between 6.9 and 7.5 are from the thiophene protons: 7.5 ppm (s, 1H), 7.36 ppm (s, 1H), 7.09 ppm (s, 1H), 6.99 ppm (s, 2H), 6.94 ppm (s, 1H). The signals smaller than 2 are related to the alkane protons: 1.6-1.2 ppm (br, 40H),1.1-0.88 ppm (m, 24H), 0.2 ppm (m, 12H). Since the simulated spectrum is only from one repeating unit and not the entire polymer, the signals in the simulated ^{1}H NMR between 2 and 3 ppm does not appear in the experimental NMR, the ppm are marked in black and of course in these positions should be bonded another repeating unit in the polymer.

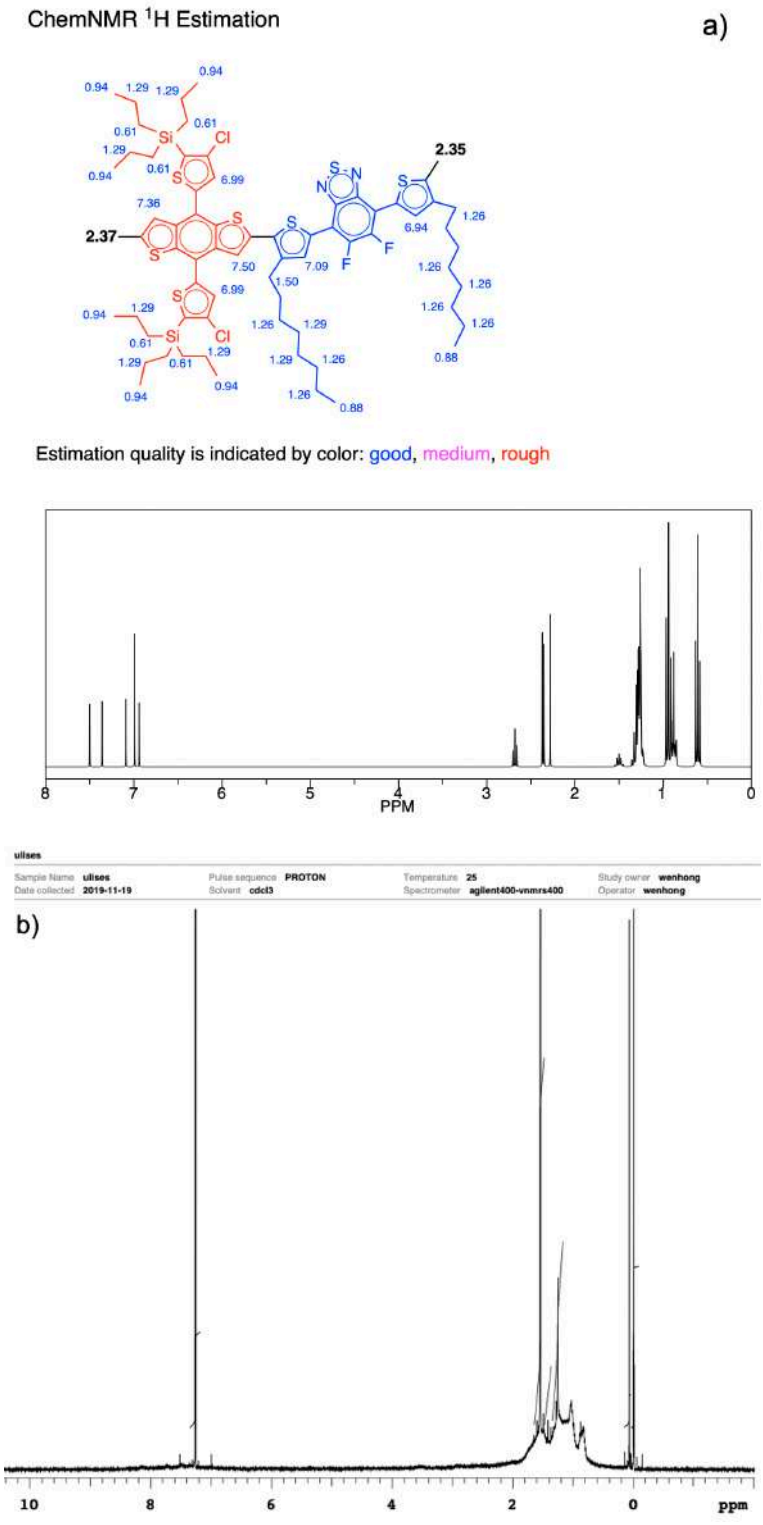

Figure 39. a) Simulated ^{1}H NMR from polymer PUM2. b) Experimental ^{1}H NMR from polymer PUM2.

With the aid of XPS and NMR it is possible to confirm the correct synthesis of the polymer, as it already was explained, the composition from XPS corresponds to

the elements of the polymer and the signals from the protons in the NMR also correspond to the designed molecular structure. As one can see, the designed structure is *ad-hoc* to be used with the GBMs, because the nine aromatic rings the repeating unit has, it will allow to strong interact by π-π stacking and therefore facilitate the exciton dissociation.

VII. Optoelectronic properties

In order to analyze the region of the solar irradiation spectrum that a material can absorb, UV-Vis is a proper technique, despite its simplicity, providing a vast amount of information. In Figure 40 a), the UV-Vis spectra from the synthesized GMBs with the polymer and in figure 40 b) the TMDs and the polymer are presented. The materials were analyzed in aqueous media dispersions, except the rGO-ODA that was analyzed in acetonitrile and the polymer which was evaluated in chloroform.

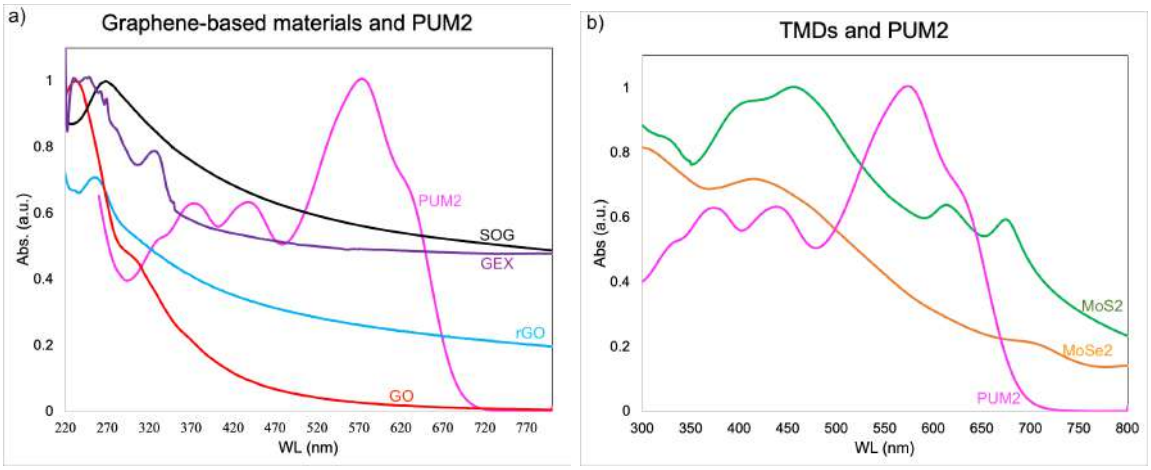

Figure 40. UV-Vis spectra from all the synthesized materials.

As can be seen, the GBMs show the maximum absorption at lower wavelengths than 370 nm. However, in all the visible spectrum SOG, GEX and rGO have a good absorption which is important for solar cell applications, this behavior could be attributed to GBMs because of the linear dispersion by Dirac´s electrons (Méndez-Romero et al., 2019). In the case of the TMDs, the maximum absorption was achieved between 350 to 500 nm which is remarkable for potential solar cell

application. It is worth to mention that both, the graphene-based materials and the TMDs have a good match with the PUM2 polymer, considering that they present complementary absorption, *i.e.*, at lower wavelengths, the 2D materials have better absorption and the polymer has good absorption from 450 nm to almost 700 nm. This represents an advantage since the higher energy will affect the polymer structure. Also, when the polymer has no absorption (>700 nm) the 2D materials still absorb in that region.

However, it is difficult to determine the absorption onset and directly deduce the bandgap from it. Therefore, in order to analyze the indirect E_g^{opt} values with a more precise approach, Tauc plots were performed and are shown in Figure 41 using the UV-Vis-NIR data. The Tauc's relation is shown in Equation 4 as follows:

$$(\alpha h\nu)^{\frac{1}{2}} = (h\nu) - E_g$$

Equation 4. Tauc's relation to calculate indirect band gap.

From Lambert Beer's law the coefficient (α) was obtained using the absorbance (*A*) and transmittance (*T*) (in Equation 5):

$$A = -Log_{10}\frac{I}{I_0} \text{ and } T = \frac{I}{I_0} = e^{-\alpha z}$$

Equation 5. Absorbance and transmittance relation to light intensity.

It can be noticed that α is described in absorbance terms, as presented in Equation 4, considering that the optical path (*z*) is equal to 1 cm:

$$\alpha = -Ln(10^{-A})$$

Equation 6. Relation between absorptivity coefficient and absorbance.

After this, we only need to convert the wavelength (λ) into energy, using the Planck's constant (*h*) in eV units and the velocity of light (*c*) (described in Equation 7):

$$E = \frac{hc}{\lambda} = h\nu$$

Equation 7. Relation between wavelength and frequency

Using the results calculated with Equations 4-7, it was possible to construct the Tauc's plot to determine the E_g^{opt} value, extrapolating a tangent line (dotted) to achieve intersection with the x axis (E_g^{opt} in eV), as shown in Figure 41.

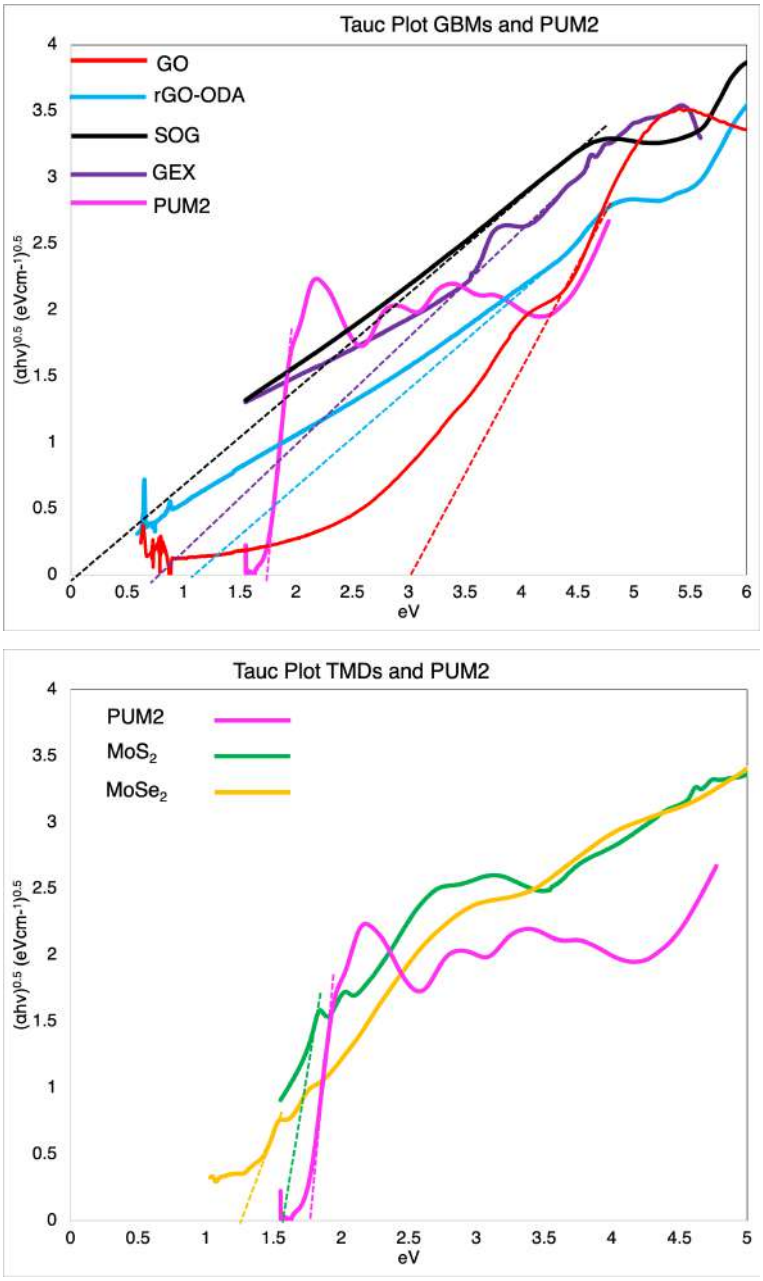

Figure 41. Tauc's plots from all the synthesized materials.

The precise determination of the optical band gap trough the Tauc plots, facilitate the analysis of the changes in such important parameter. Starting the analysis with the GBMs; from the precursor (GO), with a high band gap of 3 eV, it was possible to decrease the band gap to 1.1, 0.7 and almost 0 for rGO-ODA, GEX and SOG, respectively. These results probe the advantage of GBMs been: the easy modulation and versatility in the optical properties. For the TMDs, the obtained optical bad gaps are linked to the number of layers, being two layers for the MoS_2 and one layer for the $MoSe_2$, and the obtained values allow to use all the visible spectrum from the sun light. This is also true for the polymer PUM2, the absorption is excellent since it absorbs all the visible spectrum.

The study of energy levels corresponding to the highest occupied molecular orbital (HOMO) and the lowest unoccupied molecular orbital (LUMO) was performed with cyclic voltammetry (see Figure 42), using the onset oxidation and reduction values obtained from the cyclic voltammetry. The HOMO and LUMO values were calculated with reference against ferrocene using the following equations:

$$E_{HOMO} = -(E_{ox} + 5.13)eV$$

Equation 8. HOMO Energy determination.

$$E_{LUMO} = -(E_{red} + 5.13)eV$$

Equation 9. LUMO Energy determination.

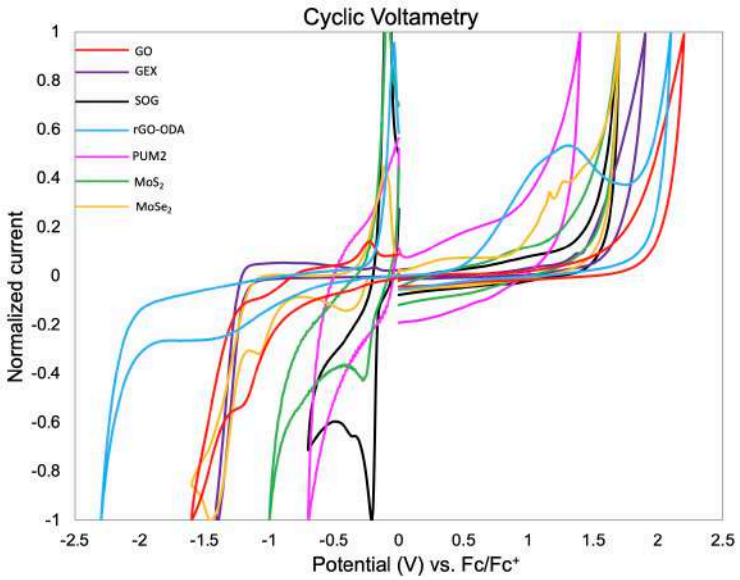

Figure 42. GO, GEX, SOG, rGO-ODA, PUM2, MoS_2 and $MoSe_2$ voltamperograms from cyclic voltammetry.

From Figure 42 it is important to see how the onsets are moving towards the 0 V, *i.e.*, the HOMO-LUMO levels are different from each sample. By definition, the electrochemical band-gap energy (E_g^{cv}) is the energy difference between HOMO and LUMO. The HOMO-LUMO values obtained from Equations 8 and 9 are summarized with all the optoelectronic properties in Table 4.

Table 4. Summary of optoelectronic properties from all the materials

Material	HOMO (eV)	LUMO (eV)	E_g^{CV} (eV)	E_g^{opt} (eV)
GO	-6.69	-4.25	2.44	3
rGO-ODA	-5.65	-4.44	1.21	1.1
SOG	-6.45	-4.98	1.47	0.04
GEX	-6.51	-4.95	1.56	0.72
MoS_2	-6.5	-4.87	1.63	1.6
$MoSe_2$	-6.01	-4.76	1.72	1.25
PUM2	-6.17	-4.67	1.5	1.72

The E_g^{cv} measured directly by cyclic voltammetry present expected discrepancies in comparison to the E_g^{opt} obtained from UV-Vis NIR data. This incongruence can be ascribed to the different method employed for the measurements. Indeed, in the CV, ionized states are generated, while after light absorption the excited state is based on electrons and holes electrostatically bound. Moreover, an energetic barrier between the electrode surface and the deposited material film can further contribute to increase the electrochemically derived energies. Finally, the resulting thin-film quality, and subsequent materials self-organization, prepared over the electrode might be different, reflecting possible variations.(Gedefaw et al., 2016)

In order to easily visualize the data from the CV measurements, an energy level diagram is presented in Figure 43. It can be notice that the polymer PUM2 has a much better band alignment with the synthesized 2D materials, which is beneficial in order to promote an exciton dissociation and preserving better energy efficiency, in this sense, it is possible to assert that the synthesized semiconducting polymer was an *ad-hoc* material tailor made for its use in conjunction with the 2D materials, not only because its aromatic structure, but the good match between the frontier orbitals, especially when compared with the conventional P3HT and PCBMs.

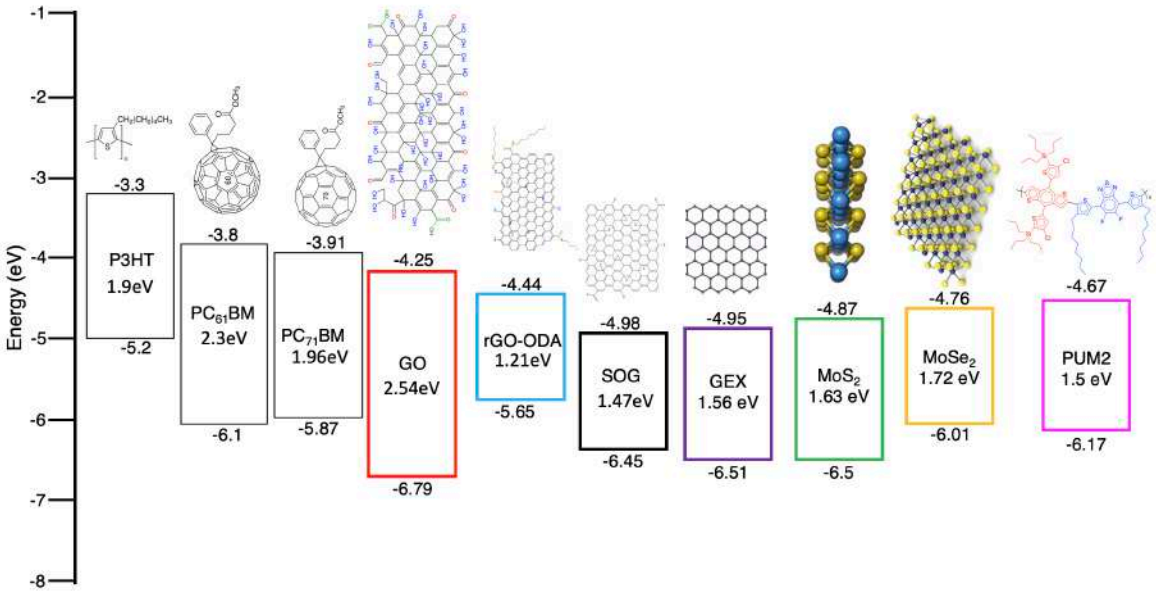

Figure 43. Energy level diagram from the synthesized materials and P3HT and PCBMs.

VIII. Electron microscopy

This section allows to assess the morphology of the synthesized 2D materials, from the raw material and after the synthesis process. In Figure 44, the SEM micrograph from the starting graphite nanoparticles (GNPs) is presented. As can be noticed, it consists of a graphitic material composed of several layers stacked together. The lateral size of this starting material is around 500 to 800 nm.

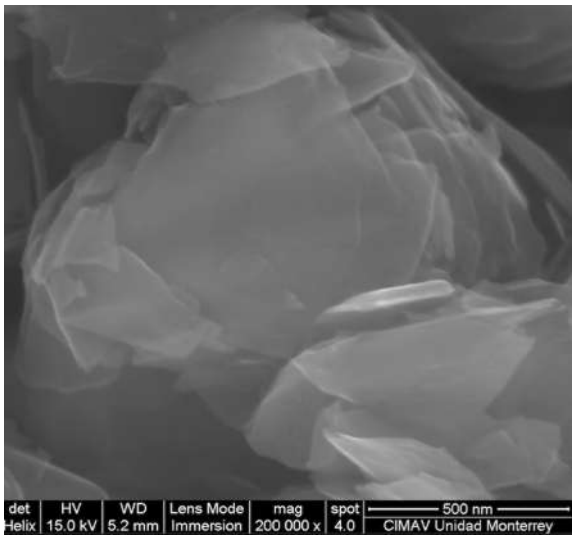

Figure 44. SEM micrograph from the starting GNPs

In the case of the precursor GO, as previously stablished, it was subjected to a lateral size reduction. In Figure 45, the micrographs from scanning transmission electron microscopy (STEM) are presented. The Figure 45 a) shows the starting GO, without any modification and the Figure 45 b) shows the GO after the ultrasonic treatment. It is clear that a lateral size reduction was achieved. In both cases, a single-layer material is displayed, with the characteristic wrinkles.

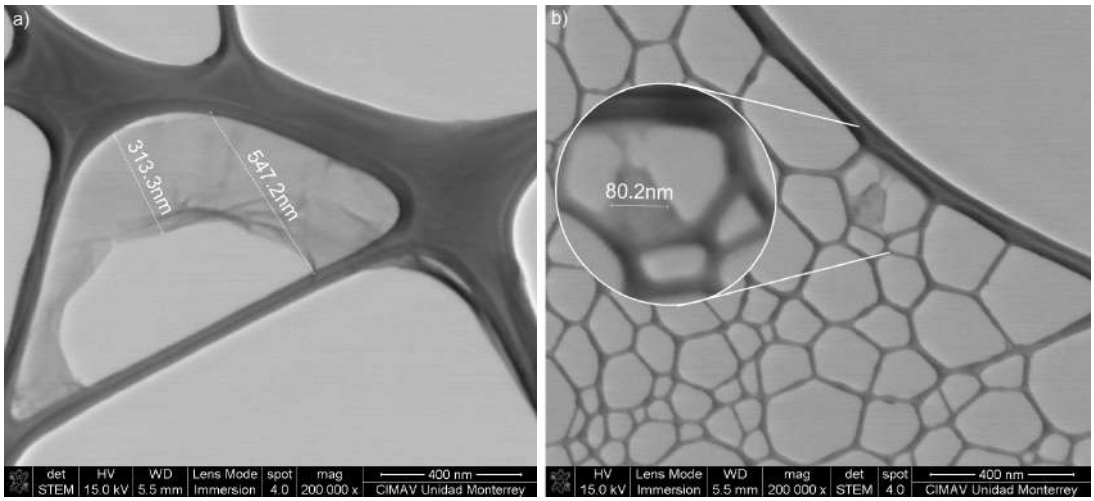

Figure 45. STEM from the GO, a) starting GO and b) GO after size reduction

The rGO-ODA, SOG and GEX are presented in Figure 46 a), b) and c) respectively. In the 3 cases, they appear flatter when compared to the GO. But in a single layer material. The lateral size is similar in the 3 type of materials been around 100 nm.

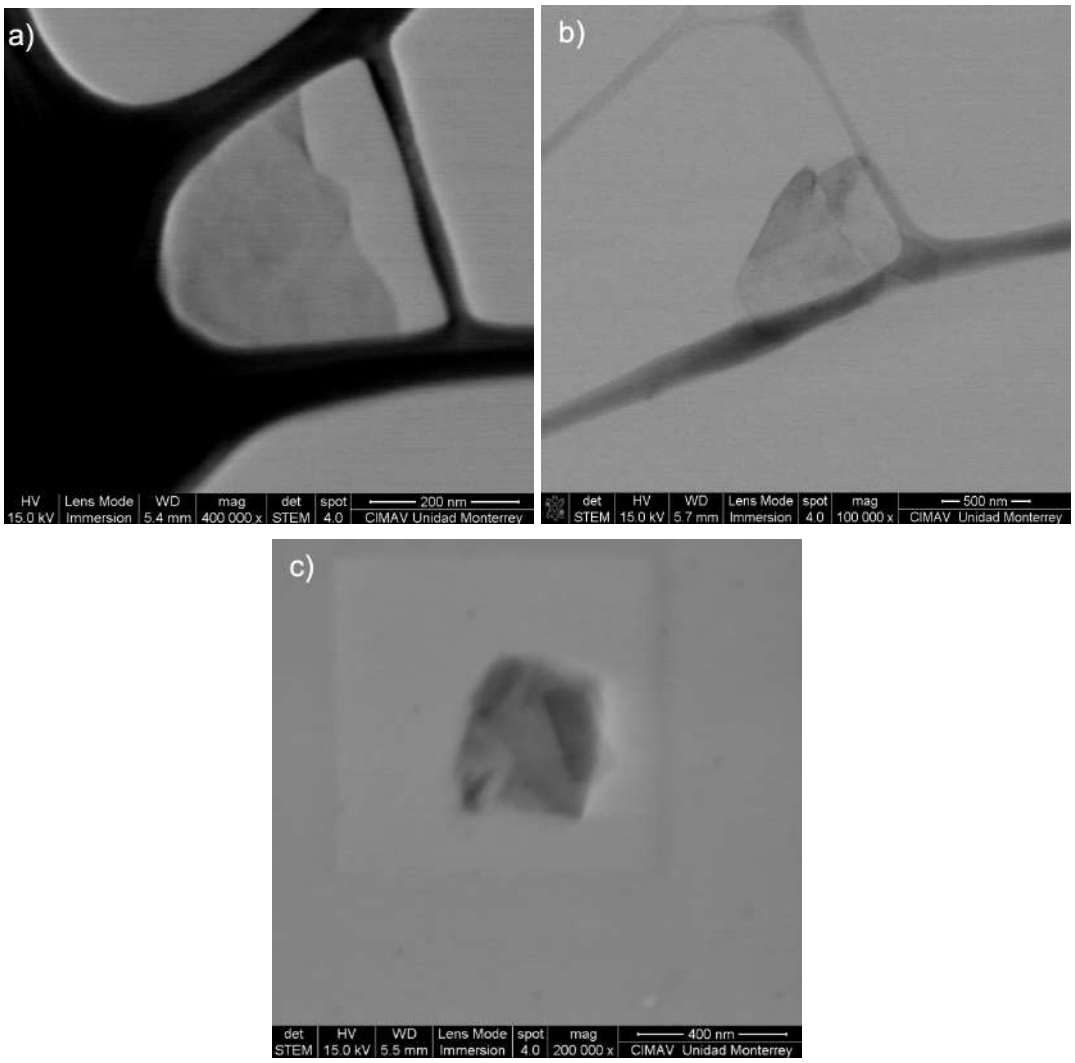

Figure 46. a) STEM micrograph from rGO-ODA. b) STEM micrograph from rGO-ODA and c) STEM micrograph from GEX.

In the case of TMDs, the starting materials were around 5 μm and several layers stacked, however, once the synthesis process was carried out, the resulting materials were few-layered and the lateral size around 300 nm, as expected for the

size reduction process. In Figure 47. The starting MoS_2 is presented and next to it is the exfoliated MoS_2.

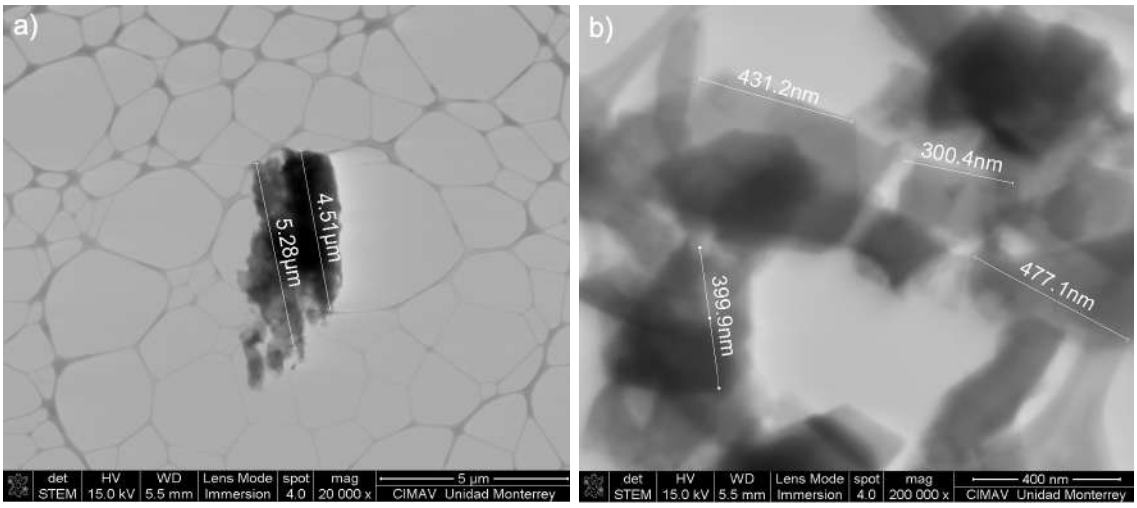

Figure 47. a) STEM micrograph from starting MoS_2 and b) STEM micrograph from exfoliated MoS_2.

IX. Organic Solar Cells

The fabricated OPVs devices, were characterized, by doing two measurements, as described in Figure 9. One measurement, in darkness is done inside a double box, and the second under direct sunlight illumination. A diagram can be seen in Figure 48. During the sunlight illumination test, the solar irradiance was monitored, being around 1069 and 1100 W m^{-2}.

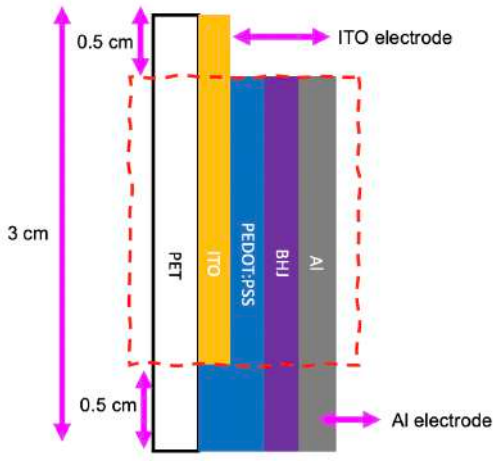

Figure 48. Diagram of the fabricated solar cells, with an active area of 4 cm^2.

In order to analyze the synthesized materials, four different BHJ devices were fabricated. In Figure 49 the four zoomed in I-V curves are shown, the zoom in is done in order to clearly see the main parameters, the dotted lines are the measurements in darkness and the solid lines are under sunlight illumination.

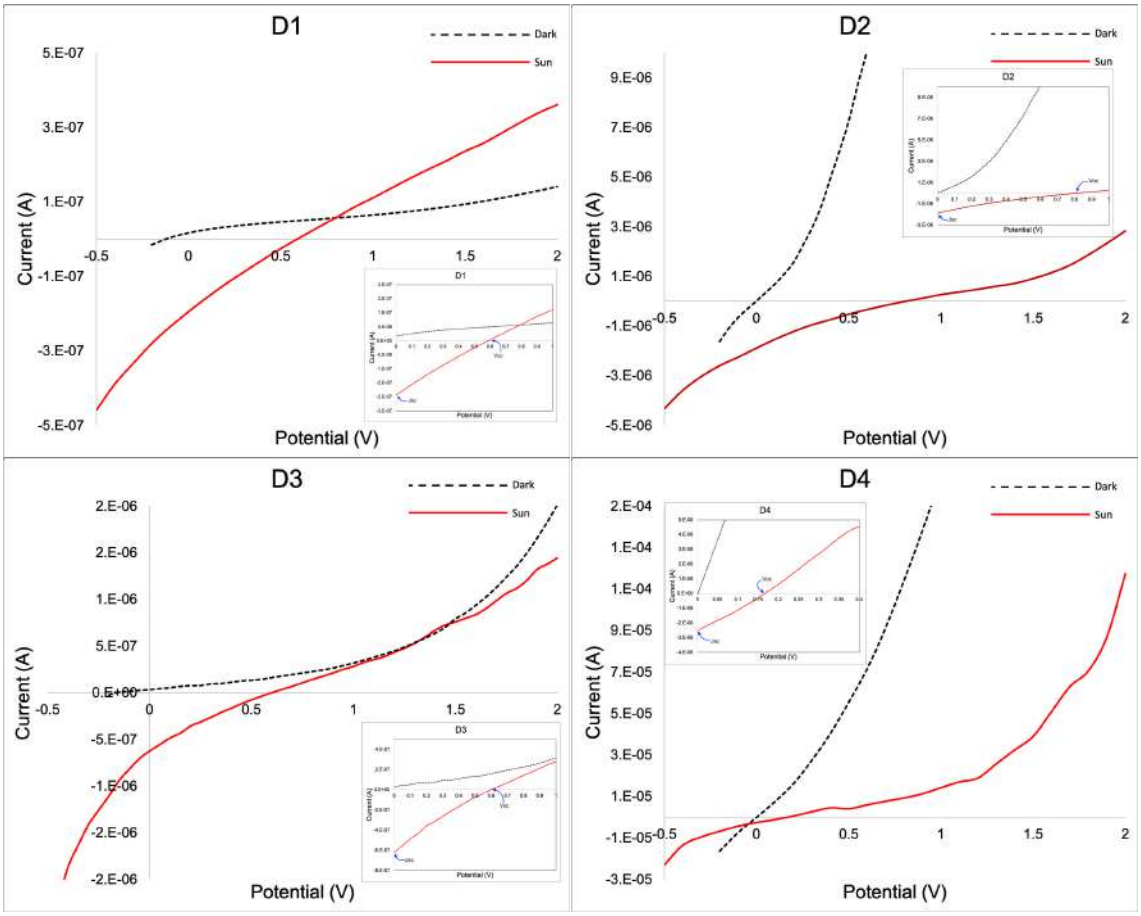

Figure 49. I-V curves from the four different type of devices.

For simplicity, the data aquired from the I-V curves are summarized in Table 5.

Table 5. Summary of OPVs results

Device	V_{OC} (V)	J_{SC} (μA)	P_{out} (μW)	PCE (%)	FF (%)
D1	0.58	0.194	0.113	0.0105	23.39
D2	0.84	0.188	0.158	0.0148	18.04
D3	0.6	0.625	0.375	0.0351	20.4
D4	0.18	2.548	0.458	0.0429	24.63

As can be seen, both in Figure 49 and in Table 5, functional devices were obtained which presented a rectifier behavior, adequate to what is expected for organic solar cells as proof of concept at laboratory level, showing that the separation of charge and current generation occur. Since the values of V_{OC} and J_{SC} are considerable high, it indicates that the charge separation takes place confirming the presented hypothesis: to be able to use this type of materials as the photoactive layer.

In general, those are very promising results than can be improved and optimized. If one carefully sees, the lowest PCE was achieved by the device D1, the commercial donor and acceptor, when the $PC_{61}BM$ was replaced by rGO-ODA, device D2 had almost 50% increase when compared to D1. Next, when PUM2 replaced the commercial P3HT in D3, it had more than 400% increase when compared to D1. Finally, when both commercial donor and acceptor, were replaced in D4, it showed an increase higher than 300% compared with D1. In the end, these results confirmed the great advantage of using 2D materials and *ad-hoc* conjugated polymer.

Of course, one can see in Table 5, that the obtained PCE is not high as expected, however, it can be attributed to multiple factors associated with the fabrication process, which was not the optimal one. The BHJ was done at ambient conditions as for the whole process, it is known that the degradation of an OPV exposed to air can dramatically decrease the PCE by 60% in few hours (Schafferhans et al., 2010). The spin coating was done with an excess of vacuum affecting the morphology and quality of the film (Holmes et al., 2019). LiF layer was not used, it is well known that LiF can improve the electron extraction dramatically (Ahlswede et al., 2007). The PCE for a similar device to D1 is around 3.5%, according to Schafferhans et al., 2010), therefore it is expected that after optimization of our process a higher value will be obtained and if it follows the tendency one can assume a four times better PCE value.

The importance in the results, is that they corroborate the feasibility of use this type of materials for photocurrent generation, a well-known mechanism is shown in Figure 50 for the process of the solar energy harvesting .

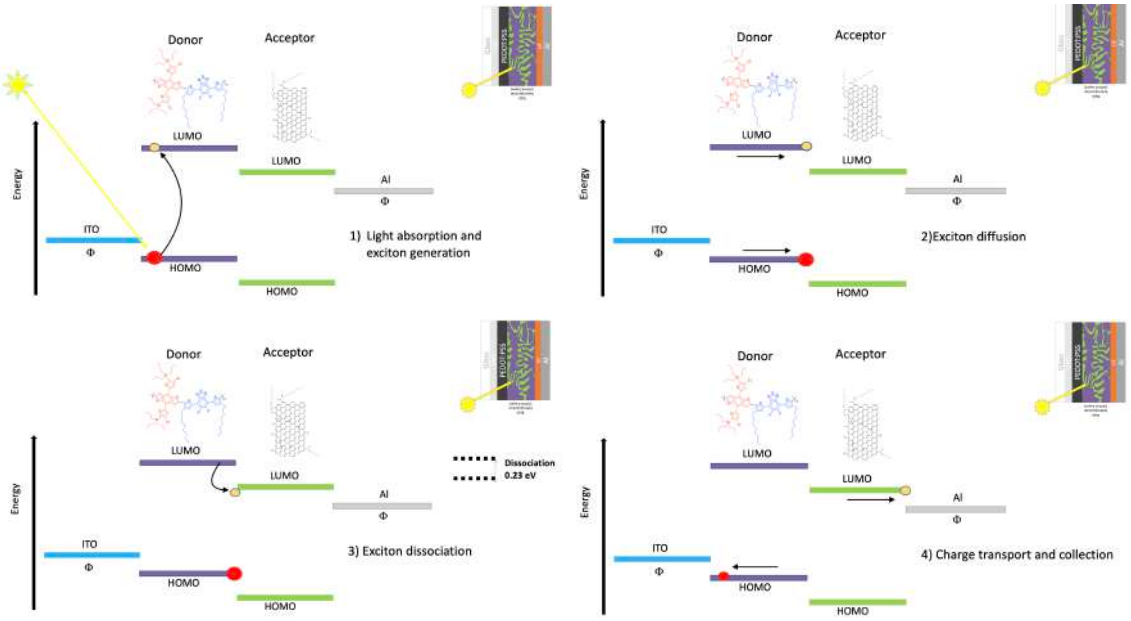

Figure 50. Photocurrent generation mechanism in the fabricated 2D materials OPVs.

X. Supercapacitors

In this project, it was proposed to combine different 2D materials, to fabricate electrodes and to produce high performance supercapacitors. Those materials show diverse characteristics with both advantages and disadvantages, but when combined, it is possible to complement each other and create a synergistic effect that will lead to a boost in energy density. Supercapacitors were fabricated in a standard Swagelock cell architecture with 8mm diameter electrodes and analyzed with a Gamry 1010E series, see Figure 51.

Figure 51. Set up to electrically characterize the supercapacitors.

To enable comparison between different electrode materials, specific capacitance values are typically normalized by either the mass of the active material (F g^{-1}), the projected electrode area (mF cm^{-2}), or volume (F cm^{-3}). However, care should be taken when comparing specific capacitance values reported in literature, as very low masses (µg) can give greatly overestimated values when extrapolated to the gram or even kilogram scale, as well as excluding the contribution of conductive additives (such as carbon black) or binding agents. Because of the difficulties in scaling up specific capacitance values for very small masses (µg or mg) of active material to large scale (g or kg) applications, the use of area normalized capacitance (mF cm^{-2}) is regarded as more accurately scalable, particularly for thin films of electrode material. The use of three-electrode systems can also exaggerate the performance of an electrode, more than doubling the measured capacitance and not accurately reflecting the performance of real-world devices(Bissett et al., 2015).

In this context, Figure 52 shows the plots of the calculated specific capacitance with increasing scan rates for each of the seven devices. As expected from Equation 3, there is a decrease in specific capacitance with increasing scan rate, due to the transport limit on the supply of ions. The GEX displays ideal EDLC behavior supported by the high discharge rate as the scan rate increases, with the

specific capacitance decreasing by only 34% when increasing the scan rate from 5 mV s^{-1} (6.2 mF cm^{-2}) up to 1000 mV/s (4.1 mF cm^{-2}). The MoS_2 membrane, however, displays high specific capacitance at low scan rates (3.5 mF cm^{-2} at 5 mV s^{-1}) but decreases by 85% at 1000 mV s^{-1} to 0.5 mF cm^{-2}, which is indicative of pseudocapacitive behavior.

In order to understand those remarkable values, it is good to compare them with a similar work. A graphene supercapacitor at 5 mV s^{-1} have 1.16 mF cm^{-2} and at 1000 mV s^{-1} it has 0.66 mF cm^{-2}. A MoS_2 supercapacitor, displayed 1.83 mF cm^{-2} at 5 mV s^{-1} but decreases by 80% at 1000 mV s^{-1} to 0.37 mF cm^{-2}.(Bissett et al., 2015) For a composite supercapacitor the specific capacitance was measured as 4.29 mF cm^{-2} at 5 mVs^{-1}; however, the composite suffers from the same degradation as seen in the pure MoS_2 device with increasing scan rate, decreasing by ~80% at 1000 mV s^{-1} to 0.98 mF cm^{-2}.(Bissett et al., 2015)

In the case of the nanocomposites (GEX+MoS_2), S4 to S7, a remarkable synergistic effect can be seen, since the highest capacitance for the S4 it is 30% greater when compared with the pure GEX and 228% higher when compare with the pure MoS_2. Surprisingly, the ternary devices, S6 and S7, does not show an increased capacitance values, but they show a better retention (~50%) at even extremely high scan rate of 50 000 mV/s, which can be attributed to the synergistic effect of the 3 components: High conductivity from GEX, redox activity from MoS_2 and both characteristics in SOG, which also will prevent the restacking. The capacitance is also shown as gravimetric in Figure 52. It is important to point out that once the capacitance is normalized to mass, the devices S4-S5 and the S6-S7 have the same values which confirms that there is not an influence in the capacitance per mass.

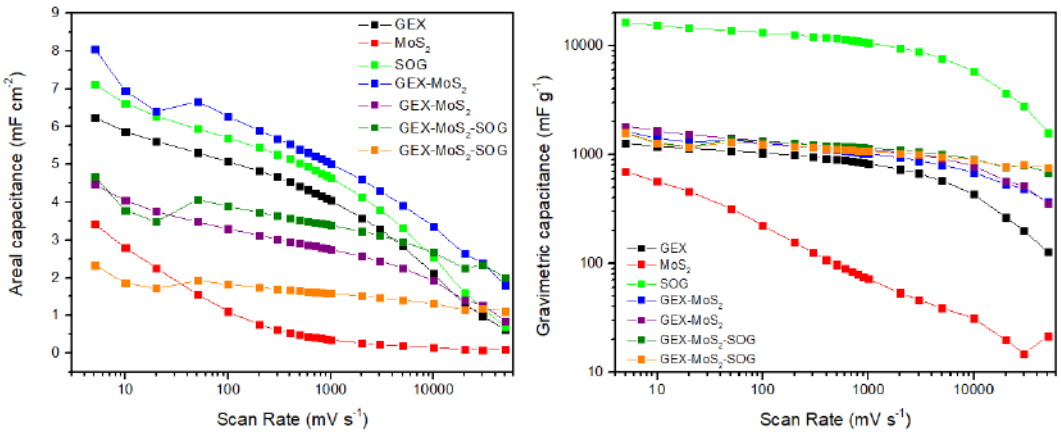

Figure 52. Supercapacitors' specific capacitance, areal and gravimetric.

The results from S3 (SOG) are very interesting, since it has better capacitance per area (16% more) than GEX, when the capacitance is analyzed in terms of mass, the SOG device has more than 13 times the capacitnace than the GEX (16 474 mF g^{-1}). It is also worth to notice the excelent retention, since even at 1000 mV s^{-1} it has more than 75% retention.

In contrast, a previous work where graphene paper (GP) and carbon nanotubes (CNTs) were grown directly to the carbon surface by CVD, forming a GP/CNT structure achieved a specific capacitance of 4.4 mF cm^{-2}, (Li, Smith, et al., 2017) which highlight the excellent results from the fabricated devices in this thesis and the synergistic effect of the used 2D materials.

In Figure 53, a schematics of the snergistic effect between the 2D materials in the electrode of a supercapacitor is shown. As can be seen, when only one type of material is used (Figure 53 a)), the ion diffusion is complicated, but the adition of different 2D materials provide better access to the active materials (Figure 53 b)).

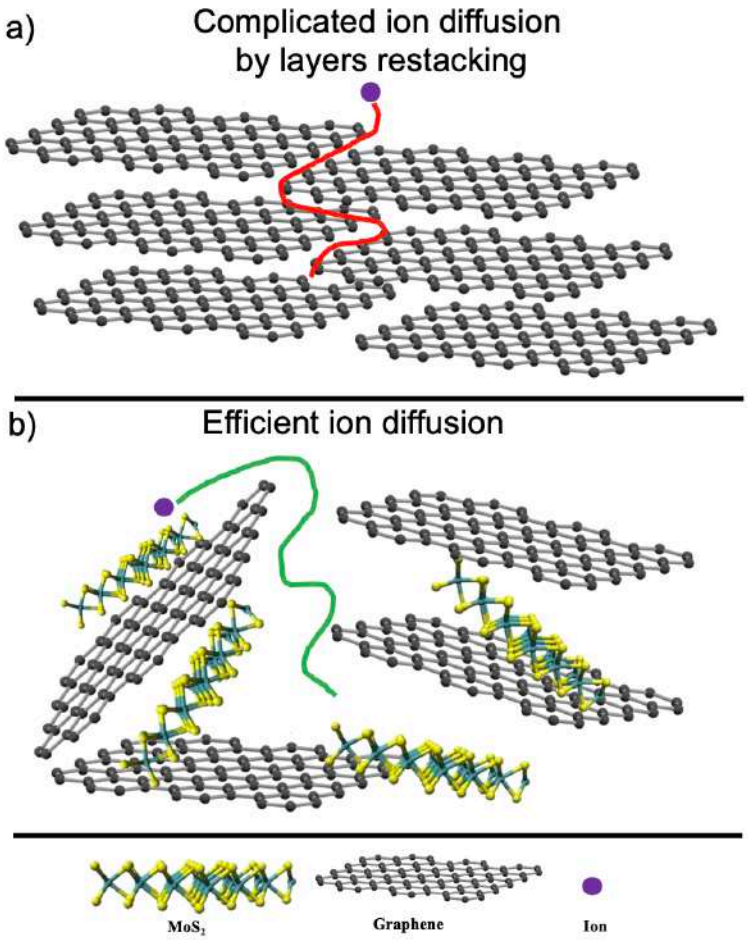

Figure 53. Schematics of the synergy between 2D materials in a supercapacitor electrode.

Conclusions

The main goal of the present work was to develop new materials and devices in order to provide solutions to the scientific and technological challenges related to the energy harvesting and storage.

Eight different materials were synthesized and modified: graphene-based materials, TMDs and a semiconducting polymer. These materials allowed the fabrication of two different type of devices for energy applications, harvesting and storage. Different devices were constructed by tailoring the properties between the different materials involved to promote a synergistic effect.

The synthesized 2D materials had the properties of size, crystallinity, solubility and number of layers controlled. It has been observed an important decrease in size above 90% from the starting 2D materials, without compromising other important parameters, such dispersibility, as well as the band gap, which are very important in order to be used as an active layer. Furthermore, the crystallinity of SOG and GEX are remarkable. The chemical structure of the investigated materials by XPS showed minimal modification and even beneficial in the case of the $MoSe_2$. Also, the XPS showed and excellent values of C/O ratio when compared with other graphene-based materials.

The synthesized semiconducting polymer, a new conjugated D-A copolymer was synthesized to have the lowest HOMO and LUMO energy levels, in order to have a better match with the energy levels from the 2D materials. It has an excellent solubility in any organic solvent, included the greener ones such as toluene or chloroform. The absorption of the polymer is good in all the UV-Vis solar spectrum.

The good solubility in organic solvents of both, the polymer and the rGO-ODA, allowed to implement a methodology to easily use them as active layer in OPVs. In the case of supercapacitors, all the materials used where soluble in water-alcohols, which simplified its use in electrodes by vacuum filtration.

The fabricated OPVs present low efficiency, however the remarkable part is that the ones made of the synthesized 2D material and the semiconducting polymer had more than 300% efficiency when compared to the OPV made with the commercial materials normally used.

For the supercapacitors, the results indicate a synergistic effect when the 2D materials are combined, which open the possibility to more architectures which eventually circumvent the 2D materials restacking issue. Initial tests show good values in specific capacity and retention for both, high scan rate and charge-discharge.

At the end, this work contributed to the development of several new functional nanomaterials and nanocomposites, it also contributed to the scientific understanding of their synthesis, modification and application. Furthermore, it paves the way for the development of new technologies, such as OPVs and supercapacitors based on 2D materials; this type of technology was greatly improved and has shown a tremendous potential after its future optimization, especially in order to mitigate problems related to the sustainable development of our society.

References

Ahlswede, E., Hanisch, J., & Powalla, M. (2007). Comparative study of the influence of LiF, NaF, and KF on the performance of polymer bulk heterojunction solar cells. *Applied Physics Letters*, *90*(16), 163504. https://doi.org/10.1063/1.2723077

Anslyn, E. V., & Dougherty, D. A. (2006). *Modern physical organic chemistry*. University science books.

Armaroli, N., & Balzani, V. (2007). The Future of Energy Supply: Challenges and Opportunities. *Angewandte Chemie International Edition*, *46*(1-2), 52-66. https://doi.org/doi:10.1002/anie.200602373

Bernardi, M., Lohrman, J., Kumar, P. V., Kirkeminde, A., Ferralis, N., Grossman, J. C., & Ren, S. (2012). Nanocarbon-Based Photovoltaics. *ACS Nano*, *6*(10), 8896-8903. https://doi.org/10.1021/nn302893p

Bernardi, M., Palummo, M., & Grossman, J. C. (2013). Extraordinary Sunlight Absorption and One Nanometer Thick Photovoltaics Using Two-Dimensional Monolayer Materials. *Nano Letters*, *13*(8), 3664-3670. https://doi.org/10.1021/nl401544y

Bissett, M. A., Kinloch, I. A., & Dryfe, R. A. W. (2015). Characterization of MoS2–Graphene Composites for High-Performance Coin Cell Supercapacitors. *ACS Applied Materials & Interfaces*, *7*(31), 17388-17398. https://doi.org/10.1021/acsami.5b04672

Boran, F., & Gürer, S. Ç. (2019). The effect of starting material types on the structure of graphene oxide and graphene. *Turkish Journal of Chemistry*, *43*, 1322-1335.

Brownson, D. A. C., Varey, S. A., Hussain, F., Haigh, S. J., & Banks, C. E. (2014). Electrochemical properties of CVD grown pristine graphene: monolayer- vs. quasi-graphene [10.1039/C3NR05643K]. *Nanoscale*, *6*(3), 1607-1621. https://doi.org/10.1039/C3NR05643K

Chen, S., Yu, X., Zhang, M., Cao, J., Li, Y., Ding, L., & Shi, G. (2015). A graphene oxide/oxygen deficient molybdenum oxide nanosheet bilayer as a hole transport layer for efficient polymer solar cells [10.1039/C5TA04823K]. *Journal of Materials Chemistry A*, *3*(36), 18380-18383. https://doi.org/10.1039/C5TA04823K

Cui, Y., Yao, H., Zhang, J., Zhang, T., Wang, Y., Hong, L., Xian, K., Xu, B., Zhang, S., Peng, J., Wei, Z., Gao, F., & Hou, J. (2019). Over 16% efficiency organic photovoltaic cells enabled by a chlorinated acceptor with increased open-circuit voltages. *Nature Communications*, *10*(1), 2515. https://doi.org/10.1038/s41467-019-10351-5

Dresselhaus, M., Jorio, A., & Saito, R. (2010). Characterizing graphene, graphite, and carbon nanotubes by Raman spectroscopy. *Annu. Rev. Condens. Matter Phys.*, *1*(1), 89-108.

Dresselhaus, M. S., Jorio, A., Hofmann, M., Dresselhaus, G., & Saito, R. (2010). Perspectives on carbon nanotubes and graphene Raman spectroscopy. *Nano Letters*, *10*(3), 751-758.

Fan, Q., Liu, T., Zhang, M., Su, W., Méndez-Romero, U. A., Yang, T., Geng, X., Hou, L., Yu, D., Liu, F., Yan, H., & Wang, E. (2020). Weak Makes It Powerful: The Role of Cognate Small Molecules as an Alloy Donor in 2D/1A Ternary Fullerene Solar Cells for Finely Tuned Hierarchical Morphology in Thick Active Layers. *Small Methods*, *4*(3), 1900766. https://doi.org/10.1002/smtd.201900766

Fan, Q., Méndez-Romero, U. A., Guo, X., Wang, E., Zhang, M., & Li, Y. (2019). Fluorinated Photovoltaic Materials for High-Performance Organic Solar Cells. *Chemistry – An Asian Journal*, *14*(18), 3085-3095. https://doi.org/10.1002/asia.201900795

Fan, Q., Su, W., Chen, S., Kim, W., Chen, X., Lee, B., Liu, T., Méndez-Romero, U. A., Ma, R., Yang, T., Zhuang, W., Li, Y., Li, Y., Kim, T.-S., Hou, L., Yang, C., Yan, H., Yu, D., & Wang, E. (2020). Mechanically Robust All-Polymer Solar Cells from Narrow Band Gap Acceptors with Hetero-Bridging Atoms. *Joule*, *4*(3), 658-672. https://doi.org/https://doi.org/10.1016/j.joule.2020.01.014

Fan, Q., Su, W., Wang, Y., Guo, B., Jiang, Y., Guo, X., Liu, F., Russell, T. P., Zhang, M., & Li, Y. (2018). Synergistic effect of fluorination on both donor and acceptor materials for high performance non-fullerene polymer solar cells with 13.5% efficiency. *Science China Chemistry*, *61*(5), 531-537. https://doi.org/10.1007/s11426-017-9199-1

Ferrari, A. C. (2007). Raman spectroscopy of graphene and graphite: Disorder, electron–phonon coupling, doping and nonadiabatic effects. *Solid state communications*, *143*(1-2), 47-57.

Garg, R., Dutta, N. K., & Choudhury, N. R. (2014). Work function engineering of graphene. *Nanomaterials*, *4*(2), 267-300.

Garg, R., Elmas, S., Nann, T., & Andersson, M. R. (2017). Deposition Methods of Graphene as Electrode Material for Organic Solar Cells. *Advanced Energy Materials*, *7*(10), 1601393. https://doi.org/10.1002/aenm.201601393

Gedefaw, D., Tessarolo, M., Bolognesi, M., Prosa, M., Kroon, R., Zhuang, W., Henriksson, P., Bini, K., Wang, E., Muccini, M., Seri, M., & Andersson, M. R. (2016). Synthesis and characterization of benzodithiophene and benzotriazole-based polymers for photovoltaic applications. *Beilstein Journal of Organic Chemistry*, *12*, 1629-1637. https://doi.org/10.3762/bjoc.12.160

Geim, A. K., & Novoselov, K. S. (2010). The rise of graphene. In *Nanoscience and technology: a collection of reviews from nature journals* (pp. 11-19). World Scientific.

Hollas, J. M. (2004). *Modern spectroscopy*. John Wiley & Sons.

Holmes, N. P., Munday, H., Barr, M. G., Thomsen, L., Marcus, M. A., Kilcoyne, A. L. D., Fahy, A., van Stam, J., Dastoor, P. C., & Moons, E. (2019). Unravelling donor–acceptor film morphology formation for environmentally-friendly OPV ink formulations [10.1039/C9GC02288K]. *Green Chemistry*, *21*(18), 5090-5103. https://doi.org/10.1039/C9GC02288K

Hou, D., Liu, Q., Wang, X., Quan, Y., Qiao, Z., Yu, L., & Ding, S. (2018). Facile synthesis of graphene via reduction of graphene oxide by artemisinin in ethanol. *Journal of Materiomics*, *4*(3), 256-265. https://doi.org/https://doi.org/10.1016/j.jmat.2018.01.002

Huang, X., Qi, X., Boey, F., & Zhang, H. (2012). Graphene-based composites [10.1039/C1CS15078B]. *Chemical Society Reviews*, *41*(2), 666-686. https://doi.org/10.1039/C1CS15078B

Jeon, Y.-J., Yun, J.-M., Kim, D.-Y., Na, S.-I., & Kim, S.-S. (2012). High-performance polymer solar cells with moderately reduced graphene oxide as an efficient hole transporting layer. *Solar Energy Materials and Solar Cells*, *105*, 96-102. https://doi.org/https://doi.org/10.1016/j.solmat.2012.05.024

Jung, I., Dikin, D. A., Piner, R. D., & Ruoff, R. S. (2008). Tunable electrical conductivity of individual graphene oxide sheets reduced at "low" temperatures. *Nano Letters*, *8*(12), 4283-4287.

Kini, G. P., Hoang, Q. V., Song, C. E., Lee, S. K., Shin, W. S., So, W.-W., Uddin, M. A., Woo, H. Y., & Lee, J.-C. (2017). Thiophene-benzothiadiazole based D–A1–D–A2 type alternating copolymers for polymer solar cells [10.1039/C7PY00696A]. *Polymer Chemistry*, *8*(23), 3622-3631. https://doi.org/10.1039/C7PY00696A

Krebs, F. C. (2008). *Polymer photovoltaics: a practical approach* (Vol. 175). SPIE press Bellingham, WA.

Lee, H. S., Min, S.-W., Chang, Y.-G., Park, M. K., Nam, T., Kim, H., Kim, J. H., Ryu, S., & Im, S. (2012). MoS2 Nanosheet Phototransistors with Thickness-Modulated Optical Energy Gap. *Nano Letters*, *12*(7), 3695-3700. https://doi.org/10.1021/nl301485q

Li, H., Wang, J., Chu, Q., Wang, Z., Zhang, F., & Wang, S. (2009). Theoretical and experimental specific capacitance of polyaniline in sulfuric acid. *Journal of Power Sources*, *190*(2), 578-586.

Li, Q., Guo, X., Zhang, Y., Zhang, W., Ge, C., Zhao, L., Wang, X., Zhang, H., Chen, J., Wang, Z., & Sun, L. (2017). Porous graphene paper for supercapacitor

applications. *Journal of Materials Science & Technology*, *33*(8), 793-799. https://doi.org/https://doi.org/10.1016/j.jmst.2017.03.018

Li, Q., Smith, A. D., Haque, M., Vyas, A., Kuzmenko, V., Lundgren, P., & Enoksson, P. (2017). Graphite paper / carbon nanotube composite: a potential supercapacitor electrode for powering microsystem technology. *Journal of Physics: Conference Series*, *922*, 012014. https://doi.org/10.1088/1742-6596/922/1/012014

Ludin, N. A., Mustafa, N. I., Hanafiah, M. M., Ibrahim, M. A., Asri Mat Teridi, M., Sepeai, S., Zaharim, A., & Sopian, K. (2018). Prospects of life cycle assessment of renewable energy from solar photovoltaic technologies: A review. *Renewable and Sustainable Energy Reviews*, *96*, 11-28. https://doi.org/https://doi.org/10.1016/j.rser.2018.07.048

Manzeli, S., Ovchinnikov, D., Pasquier, D., Yazyev, O., & Kis, A. (2017). Nature Reviews Materials 2, 17033 (2017). *URL https://doi. org/10.1038/natrevmats*.

Markavart, T., Castañer, L. (2005). *Solar Cells: Materials, Manufacture and Operation*. Elsevier.

Méndez-Romero, U. A., Pérez-García, S. A., Xu, X., Wang, E., & Licea-Jiménez, L. (2019). Functionalized reduced graphene oxide with tunable band gap and good solubility in organic solvents. *Carbon*, *146*, 491-502. https://doi.org/https://doi.org/10.1016/j.carbon.2019.02.023

Méndez-Romero, U. A., Velasco-Soto, M. Á., Licea-Jiménez, L., Álvarez-Quintana, J., & Pérez-García, S. A. (2017). Graphene derivatives: controlled properties, nanocomposites, and energy harvesting applications. In G. Z. K. a. A. C.

Mitropoulos (Ed.), *Graphene Materials - Structure, Properties and Modifications*. IntechOpen. https://doi.org/10.5772/67474

Mouri, S., Miyauchi, Y., & Matsuda, K. (2013). Tunable Photoluminescence of Monolayer MoS2 via Chemical Doping. *Nano Letters*, *13*(12), 5944-5948. https://doi.org/10.1021/nl403036h

Murto, P., Genene, Z., Benavides, C. M., Xu, X., Sharma, A., Pan, X., Schmidt, O., Brabec, C. J., Andersson, M. R., Tedde, S. F., Mammo, W., & Wang, E. (2018). High Performance All-Polymer Photodetector Comprising a Donor–Acceptor–Acceptor Structured Indacenodithiophene–Bithieno[3,4-c]Pyrroletetrone Copolymer. *ACS Macro Letters*, *7*(4), 395-400. https://doi.org/10.1021/acsmacrolett.8b00009

Novoselov, K. S., Geim, A. K., Morozov, S. V., Jiang, D., Katsnelson, M. I., Grigorieva, I., Dubonos, S., Firsov, & AA. (2005). Two-dimensional gas of massless Dirac fermions in graphene. *Nature*, *438*(7065), 197-200.

Novoselov, K. S., Geim, A. K., Morozov, S. V., Jiang, D., Zhang, Y., Dubonos, S. V., Grigorieva, I. V., & Firsov, A. A. (2004). Electric Field Effect in Atomically Thin Carbon Films. *Science*, *306*(5696), 666-669. https://doi.org/10.1126/science.1102896

Qu, S., Li, M., Xie, L., Huang, X., Yang, J., Wang, N., & Yang, S. (2013). Noncovalent Functionalization of Graphene Attaching [6,6]-Phenyl-C61-butyric Acid Methyl Ester (PCBM) and Application as Electron Extraction Layer of Polymer Solar Cells. *ACS Nano*, *7*(5), 4070-4081. https://doi.org/10.1021/nn4001963

Ru, X., Qu, M., Wang, J., Ruan, T., Yang, M., Peng, F., Long, W., Zheng, K., Yan, H., & Xu, X. (2020). 25.11% efficiency silicon heterojunction solar cell with

low deposition rate intrinsic amorphous silicon buffer layers. *Solar Energy Materials and Solar Cells*, *215*, 110643. https://doi.org/https://doi.org/10.1016/j.solmat.2020.110643

Schafferhans, J., Baumann, A., Wagenpfahl, A., Deibel, C., & Dyakonov, V. (2010). Oxygen doping of P3HT:PCBM blends: Influence on trap states, charge carrier mobility and solar cell performance. *Organic Electronics*, *11*(10), 1693-1700. https://doi.org/https://doi.org/10.1016/j.orgel.2010.07.016

Service, R. F. (2005). Is It Time to Shoot for the Sun? *Science*, *309*(5734), 548-551. https://doi.org/10.1126/science.309.5734.548

Smalley, R. E. (2005). Future global energy prosperity: the terawatt challenge. *Mrs Bulletin*, *30*(6), 412-417.

Stylianakis, M. M., Sygletou, M., Savva, K., Kakavelakis, G., Kymakis, E., & Stratakis, E. (2015). Photochemical Synthesis of Solution-Processable Graphene Derivatives with Tunable Bandgaps for Organic Solar Cells. *Advanced Optical Materials*, *3*(5), 658-666.

Subbiah, J., Purushothaman, B., Chen, M., Qin, T., Gao, M., Vak, D., Scholes, F. H., Chen, X., Watkins, S. E., Wilson, G. J., Holmes, A. B., Wong, W. W. H., & Jones, D. J. (2015). Organic Solar Cells Using a High-Molecular-Weight Benzodithiophene–Benzothiadiazole Copolymer with an Efficiency of 9.4%. *Advanced Materials*, *27*(4), 702-705. https://doi.org/10.1002/adma.201403080

Thompson, B. C., & Fréchet, J. M. J. (2008). Polymer–Fullerene Composite Solar Cells. *Angewandte Chemie International Edition*, *47*(1), 58-77. https://doi.org/http://dx.doi.org/10.1002/anie.200702506

Tongay, S., Zhou, J., Ataca, C., Lo, K., Matthews, T. S., Li, J., Grossman, J. C., & Wu, J. (2012). Thermally Driven Crossover from Indirect toward Direct Bandgap in 2D Semiconductors: MoSe2 versus MoS2. *Nano Letters*, *12*(11), 5576-5580. https://doi.org/10.1021/nl302584w

Tonndorf, P., Schmidt, R., Böttger, P., Zhang, X., Börner, J., Liebig, A., Albrecht, M., Kloc, C., Gordan, O., & Zahn, D. R. (2013). Photoluminescence emission and Raman response of monolayer MoS 2, MoSe 2, and WSe 2. *Optics express*, *21*(4), 4908-4916.

Truong, Q. D., Kempaiah Devaraju, M., Nakayasu, Y., Tamura, N., Sasaki, Y., Tomai, T., & Honma, I. (2017). Exfoliated MoS2 and MoSe2 Nanosheets by a Supercritical Fluid Process for a Hybrid Mg–Li-Ion Battery. *ACS Omega*, *2*(5), 2360-2367. https://doi.org/10.1021/acsomega.7b00379

Tsang, C. H. A., Huang, H., Xuan, J., Wang, H., & Leung, D. Y. C. (2020). Graphene materials in green energy applications: Recent development and future perspective. *Renewable and Sustainable Energy Reviews*, *120*, 109656. https://doi.org/https://doi.org/10.1016/j.rser.2019.109656

Uddin, A., & Yang, X. (2014). Surface plasmonic effects on organic solar cells. *Journal of nanoscience and nanotechnology*, *14*(2), 1099-1119. https://doi.org/10.1166/jnn.2014.9017

Vallés, C., Beckert, F., Burk, L., Mülhaupt, R., Young, R. J., & Kinloch, I. A. (2016). Effect of the C/O ratio in graphene oxide materials on the reinforcement of epoxy-based nanocomposites. *Journal of Polymer Science Part B: Polymer Physics*, *54*(2), 281-291. https://doi.org/10.1002/polb.23925

Velasco-Soto, M. A., Pérez-García, S. A., Alvarez-Quintana, J., Cao, Y., Nyborg, L., & Licea-Jiménez, L. (2015). Selective band gap manipulation of graphene oxide by its reduction with mild reagents. *Carbon*, *93*, 967-973. https://doi.org/https://doi.org/10.1016/j.carbon.2015.06.013

Volkov, A. V., Wijeratne, K., Mitraka, E., Ail, U., Zhao, D., Tybrandt, K., Andreasen, J. W., Berggren, M., Crispin, X., & Zozoulenko, I. V. (2017). Understanding the capacitance of PEDOT: PSS. *Advanced Functional Materials*, *27*(28), 1700329.

Wadsworth, A., Moser, M., Marks, A., Little, M. S., Gasparini, N., Brabec, C. J., Baran, D., & McCulloch, I. (2019). Critical review of the molecular design progress in non-fullerene electron acceptors towards commercially viable organic solar cells [10.1039/C7CS00892A]. *Chemical Society Reviews*. https://doi.org/10.1039/C7CS00892A

Wang, C., Xu, X., Zhang, W., Bergqvist, J., Xia, Y., Meng, X., Bini, K., Ma, W., Yartsev, A., Vandewal, K., Andersson, M. R., Inganäs, O., Fahlman, M., & Wang, E. (2016). Low Band Gap Polymer Solar Cells With Minimal Voltage Losses. *Advanced Energy Materials*, *6*(18), 1600148-n/a, Article 1600148. https://doi.org/10.1002/aenm.201600148

Wang, X.-Y., Narita, A., & Müllen, K. (2017). Precision synthesis versus bulk-scale fabrication of graphenes. *Nature Reviews Chemistry*, *2*(1), 0100. https://doi.org/10.1038/s41570-017-0100

Wang, Z., Yao, Q., & Eigler, S. (2020). Room-Temperature Transport Properties of Graphene with Defects Derived from Oxo-Graphene. *Chemistry – A European Journal*, *26*(29), 6484-6489. https://doi.org/10.1002/chem.201905252

Wu, Z.-S., Ren, W., Wang, D.-W., Li, F., Liu, B., & Cheng, H.-M. (2010). High-Energy MnO2 Nanowire/Graphene and Graphene Asymmetric Electrochemical Capacitors. *ACS Nano*, *4*(10), 5835-5842. https://doi.org/10.1021/nn101754k

Yu, G., Gao, J., Hummelen, J. C., Wudl, F., & Heeger, A. J. (1995). Polymer Photovoltaic Cells: Enhanced Efficiencies via a Network of Internal Donor-Acceptor Heterojunctions. *Science*, *270*(5243), 1789-1791. https://doi.org/10.1126/science.270.5243.1789

Zhang, M., Guo, X., Ma, W., Ade, H., & Hou, J. (2015). A Large-Bandgap Conjugated Polymer for Versatile Photovoltaic Applications with High Performance. *Advanced Materials*, *27*(31), 4655-4660. https://doi.org/doi:10.1002/adma.201502110

Zheng, F., Xu, W.-L., Jin, H.-D., Hao, X.-T., & Ghiggino, K. P. (2015). Charge transfer from poly (3-hexylthiophene) to graphene oxide and reduced graphene oxide. *RSC advances*, *5*(109), 89515-89520.